KLOE NOTE n.192

Measurement of $\sigma(e^+e^- \to \pi^+\pi^-\gamma)$ and extraction of $\sigma(e^+e^- \to \pi^+\pi^-)$ below 1 GeV with the KLOE detector

Achim Denig[a], Stefano Di Falco[b], Marco Incagli[b], Wolfgang Kluge[a], Debora Leone[a], Stefan Müller[a], Federico Nguyen[c], Barbara Valeriani[a], Graziano Venanzoni[b]

[a]*Institut für Experimentelle Kernphysik, Universität Karlsruhe, Germany*
[b]*Dipartimento di Fisica dell'Università e Sezione INFN, Pisa, Italy*
[c]*Dipartimento di Fisica dell'Università "Roma Tre" e Sezione INFN, Rome, Italy*

Version 5.0 - October 15, 2004

Abstract

The cross section $\sigma(e^+e^- \to \pi^+\pi^-\gamma)$ has been measured with the KLOE detector at the electron-positron collider DAΦNE, at an energy $W = m_\phi = 1.02$ GeV. From the dependence of the cross section on the invariant mass of the two-pion system we extract $\sigma(e^+e^- \to \pi^+\pi^-)$ for the mass range $0.35 < s < 0.95$ GeV^2. From this result we calculate the pion form factor and the hadronic contribution to the muon anomaly a_μ.

Contents

1 Hadronic cross section at DAΦNE

1.1 Motivation

The recent precision measurement of the muon anomaly a_μ at the Brookhaven National Laboratory [1] has led to renewed interest in accurate measurements of the cross section for e^+e^- annihilation into hadrons. Contributions to the photon spectral functions due to quark loops are not calculable for low hadronic mass states because of the failure of perturbative QCD at low energy. A very clean way out has been known for a long time [2]. The imaginary part of the hadronic piece of the spectral function is connected by unitarity to the cross section for $e^+e^- \to$ hadrons. A dispersion relation can thus be derived, giving the contribution to a_μ as an integral over the hadronic cross section multiplied by a kernel $K(s)$ which is a monotonic function that behaves approximately like $1/s$:

$$a_\mu^{\rm had} = \frac{1}{4\pi^3}\int_{4m_\pi^2}^{\infty} \sigma_{e^+e^-\to{\rm hadr}}(s)K(s){\rm d}s, \tag{1.1}$$

An example of a first complete estimate of the correction was given in the year 1985, $a_\mu^{\rm had}$=707(6)(17)$\cdot 10^{-10}$[3]. The process $e^+e^-\to\pi^+\pi^-$ below 1 GeV contributes to 62% of the total hadronic contribution [5].

The most recent measurements of $\sigma(e^+e^-\to\pi^+\pi^-)$ for values of $\sqrt{s_\pi}$ between 610 and 961 MeV come from the CMD-2 experiment at VEPP-2M, claiming a systematic error of 0.6% with a statistical error of $\sim$0.7% [4]. Their data have been used most recently together with τ and e^+e^- data up to 3 GeV to produce a firm prediction for comparison with the BNL result [6]. There is however a rather strong disagreement between the $a_\mu^{\rm had}$ value obtained using τ decay data after isospin correction and $e^+e^-\to\pi^+\pi^-$ data. Moreover the $e^+e^-\to\pi^+\pi^-$ based result disagrees by $\sim$3 σ with the direct measurement of a_μ. There are thus many reasons for new measurements of the e^+e^- annihilation cross section into two pions.

1.2 Radiative Return

Initial state radiation, ISR, is a convenient mechanism which allows studying $e^+e^-\to$ hadrons, over the entire range from 2 m_π to W, the center of mass energy of the colliding beams. In the case of interest there are complications from final-state radiation (FSR). For a photon radiated before annihilation of the e^+e^- pair, the $\pi^+\pi^-$-system energy is[1] $m_{\pi^+\pi^-} = \sqrt{W^2 - 2WE_\gamma}$, thus one learns about the coupling of an off mass shell photon of mass $m_{\pi^+\pi^-}$. For a photon radiated by the final state pions, the virtual photon coupling to the $\pi^+\pi^-$ pair has a mass W. By just counting vertices, the relative probability of ISR and FSR are of the same order. This requires very careful estimates of the two processes in order to be able to use the reaction $e^+e^-\to\pi^+\pi^-\gamma$ to extract $\sigma(e^+e^-\to\pi^+\pi^-)$. The

[1] Neglecting the small ϕ momentum.

Karlsruhe theory group has given much attention to this problem and has also developed the EVA and PHOKHARA Monte Carlo programs which are fundamental to our analysis [8, 9, 10, 11, 12, 13]. In particular the PHOKHARA Monte Carlo has been used to evaluate the ISR process (radiation function H) which is necessary to derive the hadronic cross section:

$$s_\pi \cdot \frac{d\sigma_{\pi^+\pi^-\gamma}}{ds_\pi} = \sigma_{\pi^+\pi^-}(s_\pi) \cdot H(s_\pi) \tag{1.2}$$

where $s_\pi = \mathrm{m}^2_{\pi^+\pi^-}$, which coincides with the invariant mass of the intermediate photon in case of ISR radiation only. The equation above is correct at leading order if FSR emission can be neglected. The case of NLO terms, with the simultaneous emission of ISR and FSR photons, is discussed in section 6.1.

Our present analysis, following a dedicated Monte Carlo study [7], is based on the observation of Ref. [8], that for small polar angle of the radiated photon, the ISR process vastly dominates over the FSR process. In the following we restrict ourself to studying the reaction $e^+e^- \to \pi^+\pi^-\gamma$ with $\theta_\gamma < 15^o$ or $\theta_\gamma > 165^o$. For small s_π, the di-pion system recoiling against a small angle photon will result in one or both pions being lost also at small angle. Therefore we are limited to measuring $\sigma(\pi^+\pi^-)$ for $\sqrt{s_\pi}$ >550 MeV. We will be able to investigate the cross section near threshold with 2002 data, where higher statistics and better background conditions can facilitate the analysis. This is of great importance, since there are no recent good measurements of $\sigma(\pi^+\pi^-)$ at low masses, which weigh importantly in the estimate of a_μ^{had}.

2 The KLOE detector

KLOE [17] is a typical general purpose detector for e^+e^- physics. KLOE has a cylindrical geometry and consists of a large helium based *drift chamber* (DC, [18]), surrounded by an *electromagnetic calorimeter* (EmC, [19]) embedded in a superconducting magnet ($B =$ 0.52 T). The detector design was optimized for *CP* studies in the neutral kaon system, for K mesons produced in the decay of ϕ mesons almost at rest. The hadronic cross section measurement reported in the following heavily relies on the drift chamber. Its large dimensions (3.3 m length, 2 m radius) and the use of Helium gas, allow measuring momenta and direction of charged particles with high precision: $\sigma_{p_\perp}/p_\perp \leq 0.4\%$ for large angle tracks.

The EmC is made of a matrix of scintillating fibres embedded in lead, which results in a good energy resolution, $\sigma_E/E = 5.7\%/\sqrt{E(GeV)}$, and excellent timing resolution $\sigma_t = 54\ \mathrm{ps}/\sqrt{\mathrm{E(GeV)}} \oplus 50$ ps. The EmC consists of a barrel and two endcaps which surround the cylindrical DC; this gives hermetic coverage of the solid angle (98%). The presence of permanent quadrupole magnets close to the interaction point, below $\approx 20^o$, prevents small angle photon detection.

The KLOE detector is located in one of the two interaction points of the DAΦNE collider running at $W \simeq m_\phi \simeq 1019.4$ MeV/c^2. The two beams of electrons and positrons cross at an angle of 12.5 mrad, resulting in a net momentum to the ϕ meson of $p_t \simeq$ 13 MeV/c . The precise values of these quantities are monitored on a run by run basis using Bhabha events. The intrinsic CM energy fluctuation of the machine is 350 keV.

3 Event selection

The excellent KLOE resolution allows us to efficiently select $\pi^+\pi^-\gamma$ events, without explicit photon detection, because of their clean signature: Two high momentum tracks from the interaction point. For $e^+e^-\to\pi^+\pi^-\gamma$ events, θ_γ is defined as the photon polar angle, while θ_Σ is the polar angle of the two pions system, $\mathbf{p}_+ + \mathbf{p}_-$. If no additional radiation is emitted, $\theta_\gamma = 180^o - \theta_\Sigma$ (neglecting the small ϕ momentum).

3.1 The Fiducial Volume

The fiducial volume for $\pi^+\pi^-\gamma$ events has been chosen in order to minimize the relative contribution of background processes, in particular the $\phi\to\pi^+\pi^-\pi^0$ decay, which has a cross section $\simeq$ 2 orders of magnitude larger than the signal, and the process $e^+e^-\to\pi^+\pi^-\gamma$ in which the photon is emitted by one of the two final state pions (*final state radiation*, FSR).

In the first process, the three pions are preferably emitted in the central region, while in FSR the photon tends to follow the pion direction. In order to suppress those events, we define the fiducial volume as: $50^o < \theta_\pi < 130^o$ and $\theta_\Sigma < 15^o$ or $\theta_\Sigma > 165^o$, where θ_π is the polar angle of each pion. These requirements ensure high statistics for the signal and low background contamination. With this definition, no explicit tag on the photon is required, nor are events rejected if photons are present.

3.2 Selection Algorithm

3.2.1 Topological cuts

The two tracks must form a vertex close to the interaction point. We require that the vertex coordinates x_V, y_V, z_V satisfy $\sqrt{(x_V^2+y_V^2)} \le 8$ cm and $|z_V| \le 7$ cm. Additionally the tracks should have the first hit in the drift chamber with a radius in the transverse plane $\rho_{FH} = \sqrt{x_{FH}^2+y_{FH}^2} < 50$ cm and a point of closest approach to the beam line with $\rho_{PCA} = \sqrt{x_{PCA}^2+y_{PCA}^2} < 8$ cm and $|z_{PCA}| < 7$ cm. We also require $p_t > 160$ MeV or $p_z > 90$ MeV to reject spiraling tracks.

The selection efficiency of these requirements ranges from 90% to 95% and has been studied by Monte Carlo and using a data sample of $\phi\to\pi^+\pi^-\pi^0$ and $e^+e^-\to\pi^+\pi^-$ decays.

3.2.2 Pion identification

In order to reject background from $e^+e^-\to e^+e^-\gamma$, a particle ID method has been developed, using approximate likelihood estimators which are effective at separating pions from electrons. The likelihood estimators are based on time-of-flight versus momentum comparison and on the shape and energy deposition of the EmC clusters produced by charged tracks. The following likelihood functions have been built using actual data: One, L_π, to test the pion hypothesis (using $\pi^+\pi^-\pi^0$ events) and another, L_e, to test the electron hypothesis (using Bhabha events). In the case of the pion likelihood, two different functions are built, one for π^+ and one for π^-, since the energy deposition of the two particles is different, in particular at these energies. We use as discriminating variable $\zeta = \log(L_\pi/L_e)$

and we accept as pions particles with $\zeta > 0$ (see Fig. 1). The efficiency averaged over s_π is 98% for pions, while only 3% of the electrons survive rejection. Requiring pion ID for both particles (AND) leads to a 5% loss of signal events, but the sample is free of background. The AND condition is used for evaluating background. In order to count events as signal, we are requiring pion ID for at least one of the two particles (OR) with some small residual background, which has to be evaluated (see Sec. 4.1). This yields a very high efficiency for the signal and thus allows not to perform a correction for the pion ID inefficiency (see Sec. 4.2.5). A more detailed discussion on the pion ID method can be found in [28].

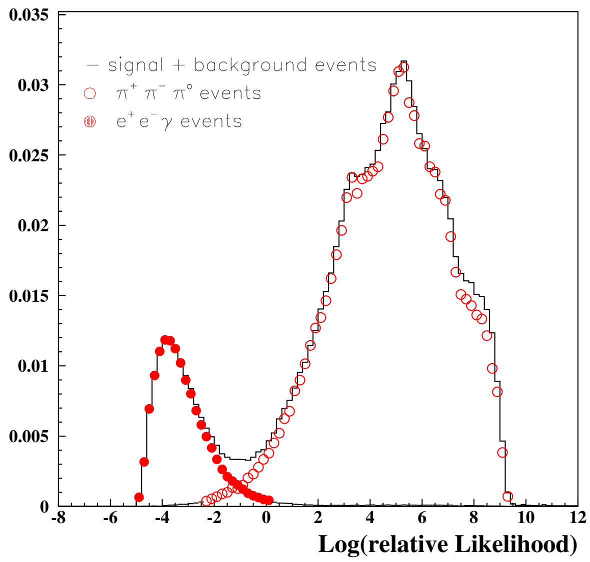

Figure 1: Distribution of the particle ID variable $\zeta = \log(L_\pi/L_e)$ for pions, right peak, and electrons, left peak.

3.2.3 Kinematic Cuts

For an $x^+x^-\gamma$ final state, momentum and energy conservation allow us to compute the mass of x, which we call m_{trk} (*trackmass*) from

$$\left(W - \sqrt{\mathbf{p}_+^2 + m_{trk}^2} - \sqrt{\mathbf{p}_-^2 + m_{trk}^2}\right)^2 - (\mathbf{p}_+ + \mathbf{p}_-)^2 = 0 \tag{3.1}$$

For $e^+e^- \to x^+x^-\gamma$, the value of m_{trk} peaks at m_π, m_μ, m_e, if $x = \pi, \mu, e$ respectively, thus allowing the selection of the signal events. The density distribution of the two track events in the [s_π,m_{trk}] plane is very effective for separating signal from background. The distribution is shown in Fig. 2 together with the selection cut defined by:

$m_{trk} > 120$ MeV $\odot\, \mathrm{m_{trk}} < 250\ \mathrm{MeV} - 105\ \mathrm{MeV} \cdot \sqrt{1 - (\mathrm{s}_\pi/0.85\mathrm{GeV}^2)^2} \odot \mathrm{m_{trk}} < 220$ MeV. In the plot, $\pi^+\pi^-\pi^0$ events are distributed in a band in the plane. The events in the signal region with $m_{trk} > 140$ MeV are due to additional ISR or FSR radiation. In particular an additional FSR photon, being emitted at large θ angle, shifts the distribution to larger values of m_{trk}. The cut on m_{trk} rejects a fraction of these events. The implications will be discussed in Sec. 6.1..

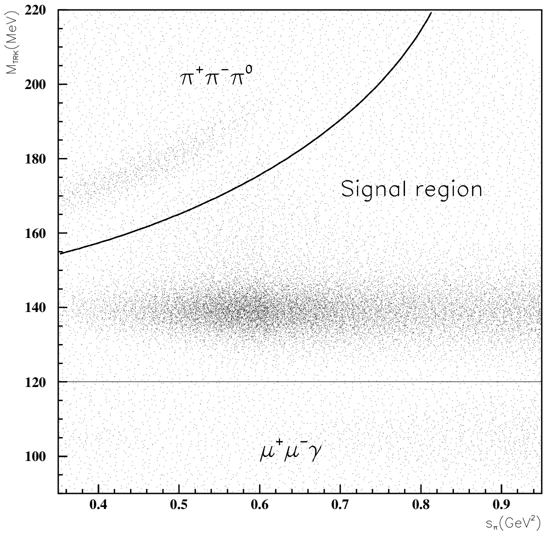

Figure 2: Kinematic separation in the $[s_\pi, m_{trk}]$ plane, of signal and backgrounds after requiring pion ID for at least one particle.

4 Event Analysis

Data were taken from July to December 2001, yielding an integrated luminosity of $L = 141.4\ \mathrm{pb}^{-1}$. After fiducial volume and selection cuts we find 1.555×10^6 events, corresponding to $\simeq 11000$ evts/pb^{-1}. Fig. 3 shows the distribution of the $\pi^+\pi^-\gamma$ events in bins of 0.01 GeV^{-2} for s_π. The ρ peak and the $\rho - \omega$ interference structure are clearly visible, even without unfolding the spectrum for the detector resolution, demonstrating the excellent momentum resolution of the KLOE detector. To obtain the cross section for $0^o < \theta_\pi < 180^o$ and $\theta_\Sigma < 15^o$ (or $\theta_\Sigma > 165^o$), we subtract the residual background from this spectrum and divide by the selection efficiency, acceptance and the integrated luminosity:[2]

$$\frac{d\sigma_{\pi\pi\gamma}}{ds_\pi} = \frac{\Delta N_{Obs} - \Delta N_{Bkg}}{\Delta s_\pi} \cdot \frac{1}{\epsilon_{Sel}\epsilon_{Acc}} \cdot \frac{1}{\int \mathcal{L} dt} \tag{4.1}$$

[2]For reasons of simplicity, the effect of unfolding has been neglected in Eq. 4.1. This effect is discussed in Sec. 4.3.

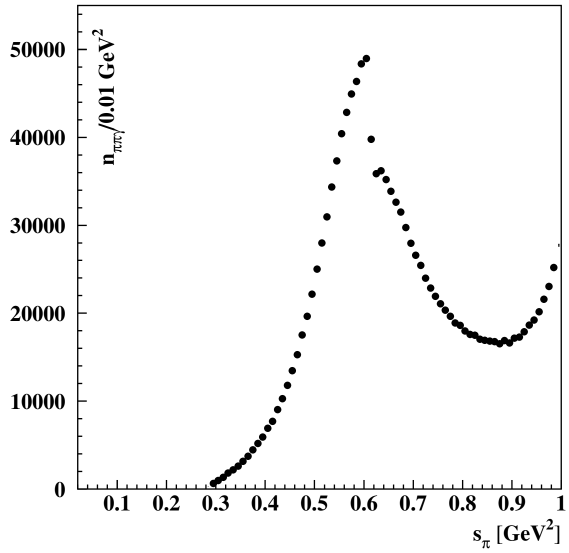

Figure 3: Distribution of counts as a function of s_π, in bins of 0.01 GeV^2, after fiducial volume and selection cuts. $L = 141.4$ pb^{-1}; data from 2001.

A sketch of the analysis flow is shown in Fig. 4.

4.1 Background subtraction

After cutting on fiducial volume, pion ID and m_{trk}, residual background of $e^+e^-\gamma$, $\mu^+\mu^-\gamma$ and $\pi^+\pi^-\pi^0$ events remains. The $[s_\pi$,$m_{trk}]$ plane population of signal and background events is illustrated in Fig. 2. The content of the two radiative background sources has been estimated using m_{trk}distributions, while that from the decay $\phi \to \pi^+\pi^-\pi^0$ is retrieved from histograms of the missing mass $m^2_{miss} = (p_\phi - p_+ - p_-)^2$, *i.e.* the four momentum conservation under the hypothesis of a final state made up of two charged pions and some missing energy.

4.1.1 Estimate of fractions of $e^+e^-\gamma$ and $\mu^+\mu^-\gamma$ events

Background from $e^+e^-\gamma$ and $\mu^+\mu^-\gamma$ events is concentrated at low values of m_{trk}. The amount of background in the signal region is obtained [21] by fitting the m_{trk} spectrum of the selected events, in slices of s_π. This is done in order to be able to reweigh, for each s_π slice, the events of the background sample as a function of s_π, after the analysis chain of Fig. 4.

The m_{trk} spectra for signal and $\mu^+\mu^-\gamma$ events are obtained from Monte Carlo samples. Reconstructed momenta from these Monte Carlo samples have been corrected to achieve agreement between data and Monte Carlo m_{trk} distributions. The corrections are such that the peak value of m_{trk} gets shifted by ~ 0.7 MeV and the width of the Monte Carlo distribution is adjusted to reproduce the width of the data distribution (see [30] for further

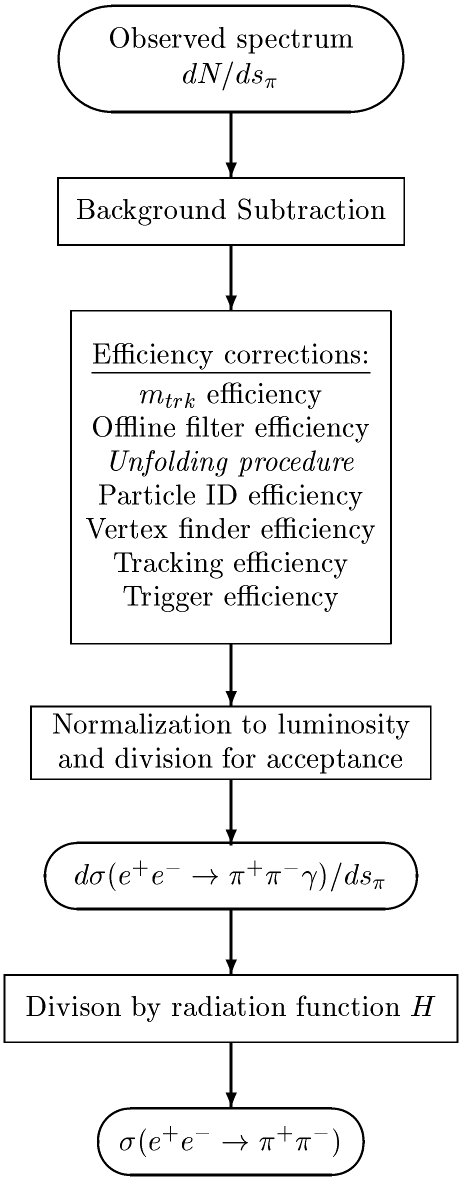

Figure 4: Analysis flow of the measurement. The order of the efficiency corrections represents the one in which the corrections have actually been performed in the analysis (see [30]). The treatment of final state radiation has been omitted for simplicity. It is explained in Sec. 6.1.

details). For $e^+e^-\gamma$ events the m_{trk} shape has been obtained from a sample of 152 pb^{-1} of data taken in 2001, selected with both tracks having $\zeta < 0$. In this way a large amount of statistics is available and the work of tuning Monte Carlo distributions to reproduce data is avoided.

First, in order to enhance the sensitivity to the small $e^+e^-\gamma$ contamination, a sample of 121 pb^{-1} of data has been fitted which had been selected according to the requirement of pion ID for one and only one track (XOR). The underlying hypothesis is that this is the only configuration in which $e^+e^-\gamma$ events are present in the selection. Some examples of the fit are shown in Fig. 5. Then, once the $e^+e^-\gamma$ content is known, it can be subtracted from the observed data sample. The obtained spectrum then is fitted according to the hypothesis that the only remaining source of background is made up of $\mu^+\mu^-\gamma$ events. Some examples of this different pattern of fits are shown in Fig. 6.

4.1.2 Estimate of fraction of $\pi^+\pi^-\pi^0$ events.

Background from $\pi^+\pi^-\pi^0$ events appears at high m_{trk} values, and, different from the bremsstrahlung processes, has a peak structure that changes with s_π, while, for every s_π range, m_{miss} peaks at m_{π^0}.

The number of $\pi^+\pi^-\pi^0$ events is obtained by fitting m_{miss} spectra with the shapes obtained from the Monte Carlo simulation, after correcting its reconstructed momenta. Moreover, the Monte Carlo $\pi^+\pi^-\pi^0$ sample has been corrected in order to generate the expected distribution of the angle between the normal axis to the plane of the event and the beams axis as described in [31].

4.1.3 Background results.

The contribution of the background from $e^+e^-\gamma$ and $\mu^+\mu^-\gamma$ estimated by means of fitting m_{trk} spectra in the range $m_{trk} \in [93, 138]$ MeV and that of the background from $\pi^+\pi^-\pi^0$ estimated by means of fitting m_{miss} spectra in the range $m_{miss} \in [70, 160]$ MeV are evaluated and shown in Fig. 8.

4.1.4 Background systematics

The systematic uncertainty on the procedure for estimating the background has been considered [22] as the error on the coefficient, w_b, used to reweigh the three samples of processes discussed above. Moreover, if the fits used to estimate w_b exhibit a probability of finding $\chi^2 > \chi^2_{min}$ smaller than 5%, the error has been stretched according to the following formula: $\delta w_b \to \delta w_b \sqrt{\chi^2_{min}/ndf}$.

4.1.5 Further background contributions

Other possible sources of considered systematics are the interaction $e^+e^- \to e^+e^-\pi^+\pi^-$ with the electrons going down the beam pipe [23] and the NLO order corrections to the FSR in the process $e^+e^- \to \mu^+\mu^-\gamma$

$\boldsymbol{e^+e^- \to e^+e^-\pi^+\pi^-}$

The Feynman diagrams contributing to this process are drawn in Fig. 9.

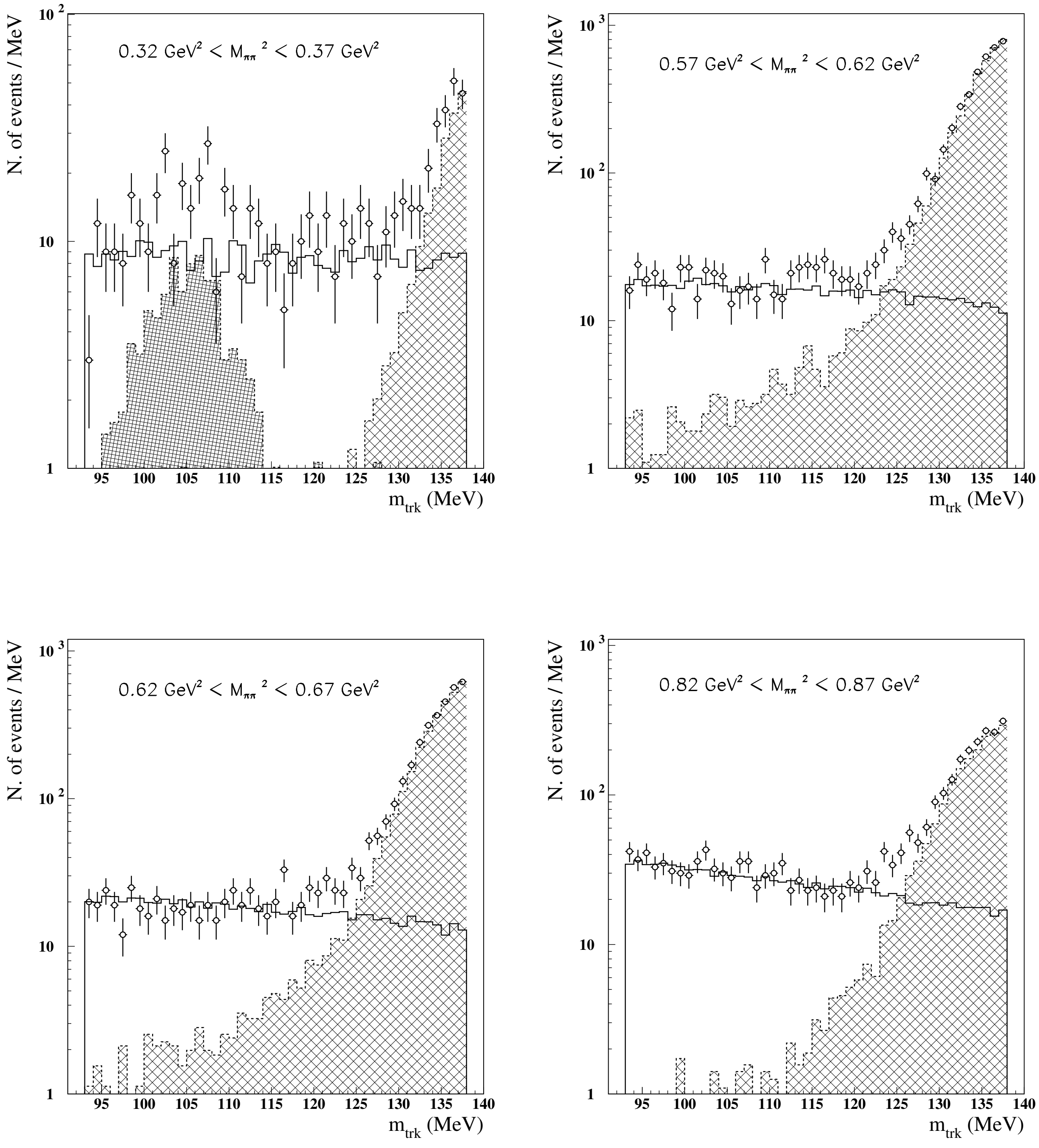

Figure 5: The m_{trk} spectrum for different s_π ranges. The samples shown are data (empty circles), reweighted MC-$\pi^+\pi^-\gamma$ (light filled histogram), reweighted $e^+e^-\gamma$from data (empty histogram) and reweighted MC-$\mu^+\mu^-\gamma$ (dark filled histogram).

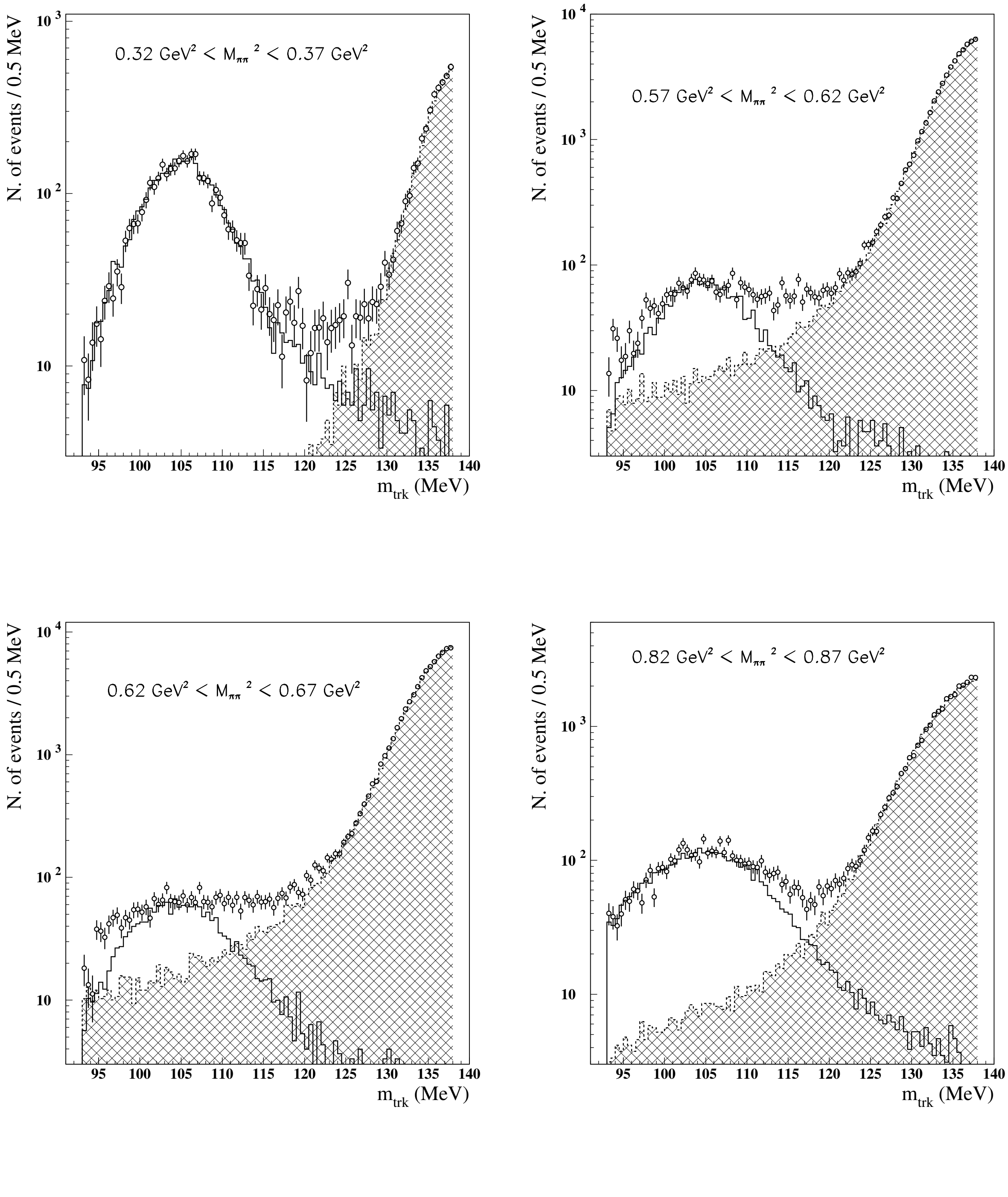

Figure 6: The m_{trk} spectrum for different s_π ranges. The samples shown are data after the $e^+e^-\gamma$ subtraction (empty circles), reweighted MC-$\pi^+\pi^-\gamma$ (filled histogram) and reweighted MC-$\mu^+\mu^-\gamma$ (empty histogram).

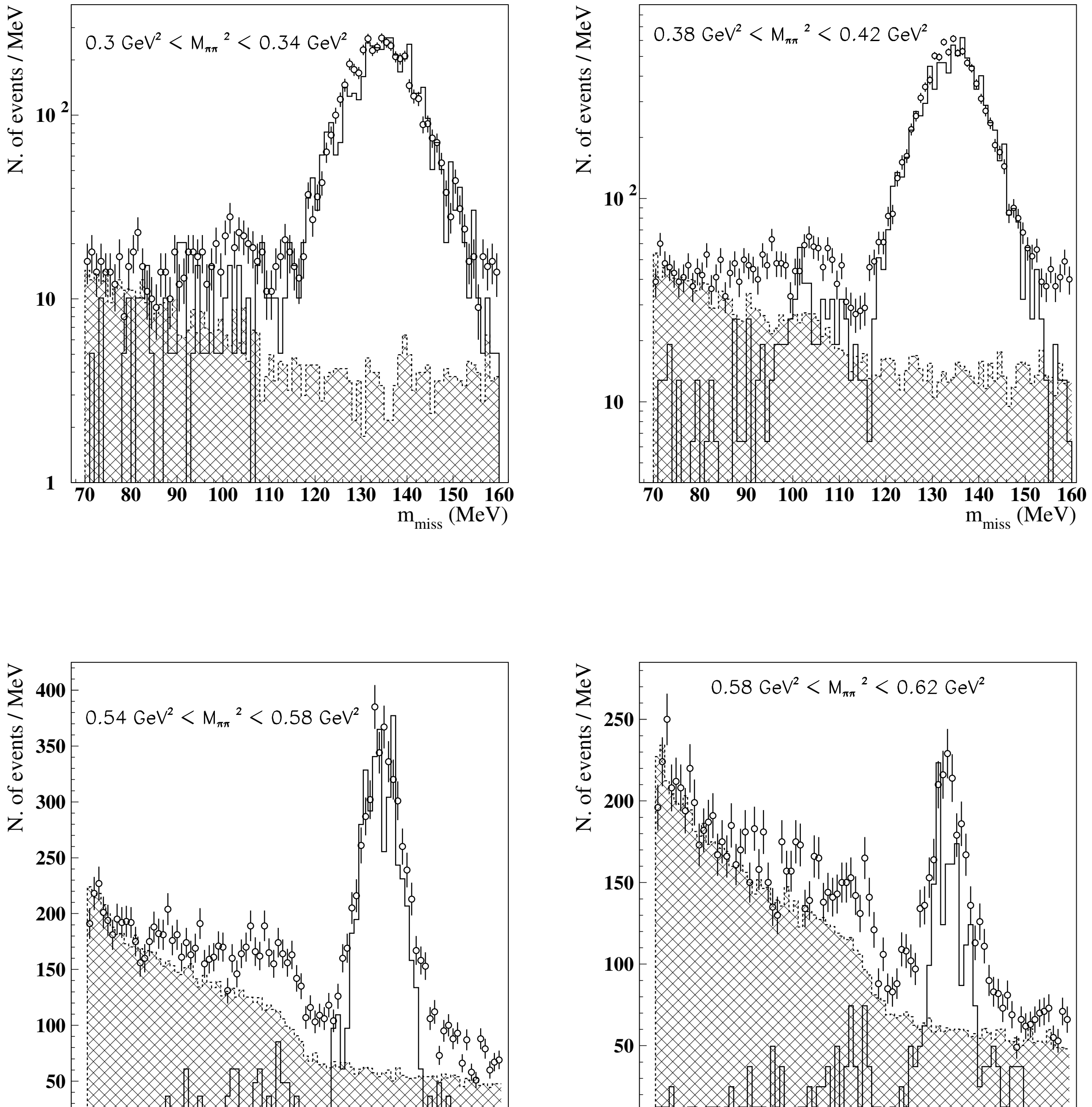

Figure 7: The m_{miss} spectrum for different s_π ranges. The samples shown are data (empty circles), reweighted MC-$\pi^+\pi^-\gamma$ (filled histogram) and reweighted MC-$\pi^+\pi^-\pi^0$ (empty histogram).

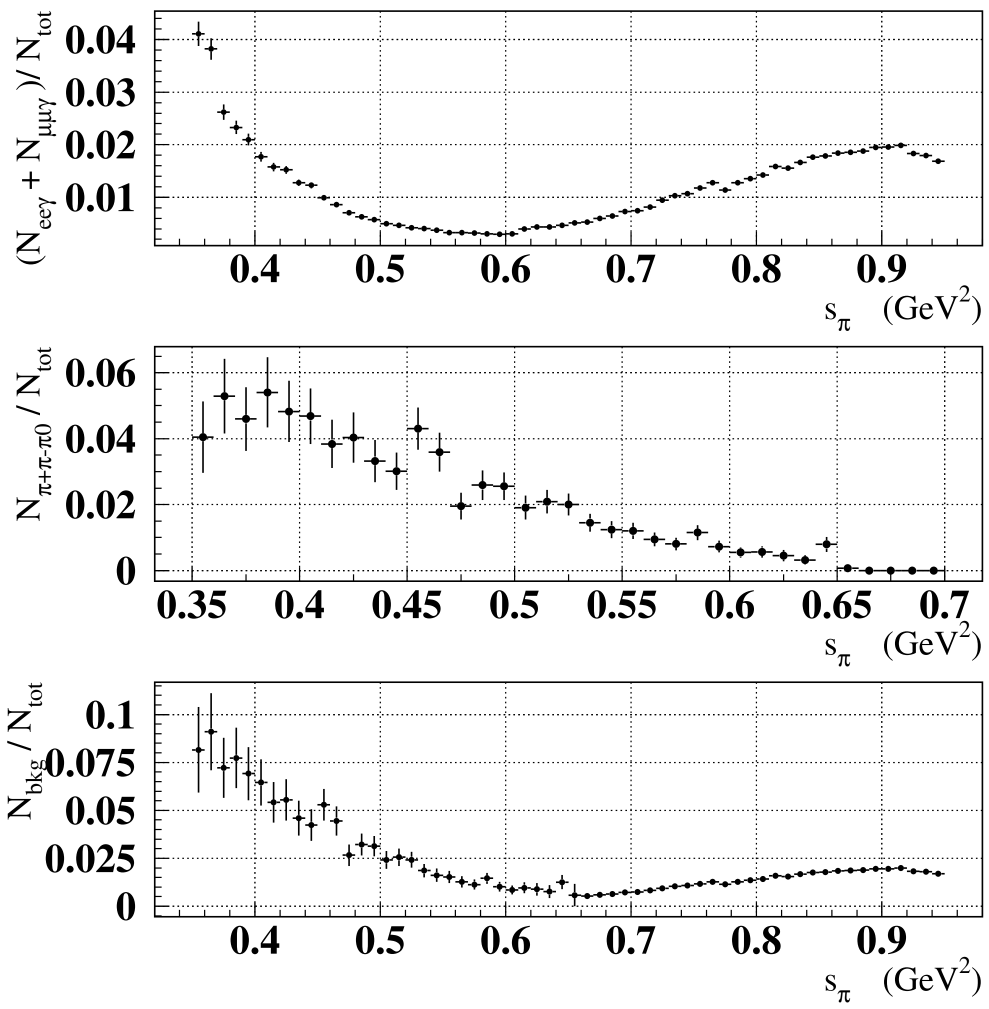

Figure 8: Fractions of $\mu^+\mu^-\gamma$, $e^+e^-\gamma$ and $\pi^+\pi^-\pi^0$ events as a function of s_π. Errors take account of the MC statistics, the uncertainty of the reweighing coefficients and the statistics of the data sample used for the fits and taken as the normalizing s_π spectrum. In addition errors coming from the fractions of $\mu^+\mu^-\gamma$ and $e^+e^-\gamma$ events are added linearly because of the correlation between the two sources of background. The lowest plot is the fraction of total background.

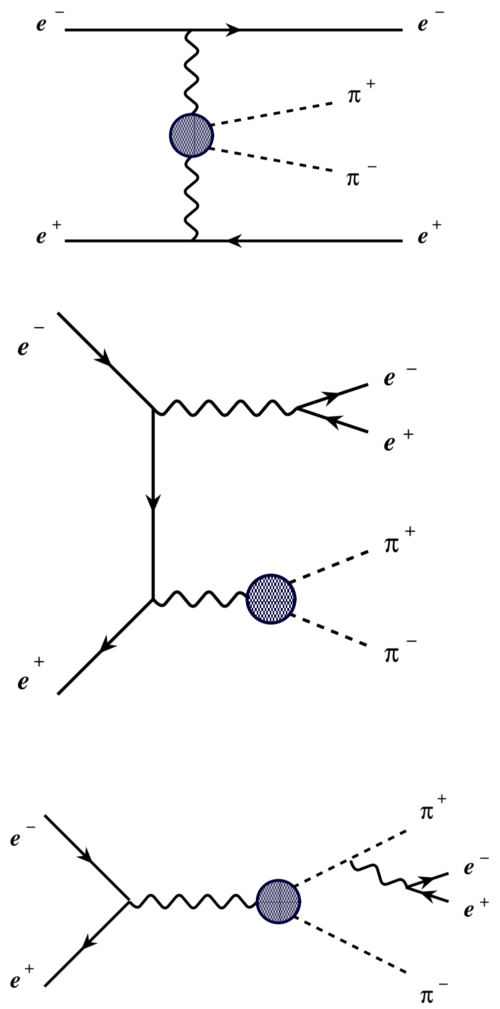

Figure 9: Background contributions from processes $e^+e^- \to e^+e^-\pi^+\pi^-$.

The upper diagram, often referred as the photon photon fusion contribution, has been studied by means of a Monte Carlo code developed by F. Anulli and A. Courau [24] for the reactions $\gamma\gamma \to hadrons$. After applying the cuts on the polar angle of pions and of the dipion system and on m_{trk} , the ratio of this contribution to the signal is

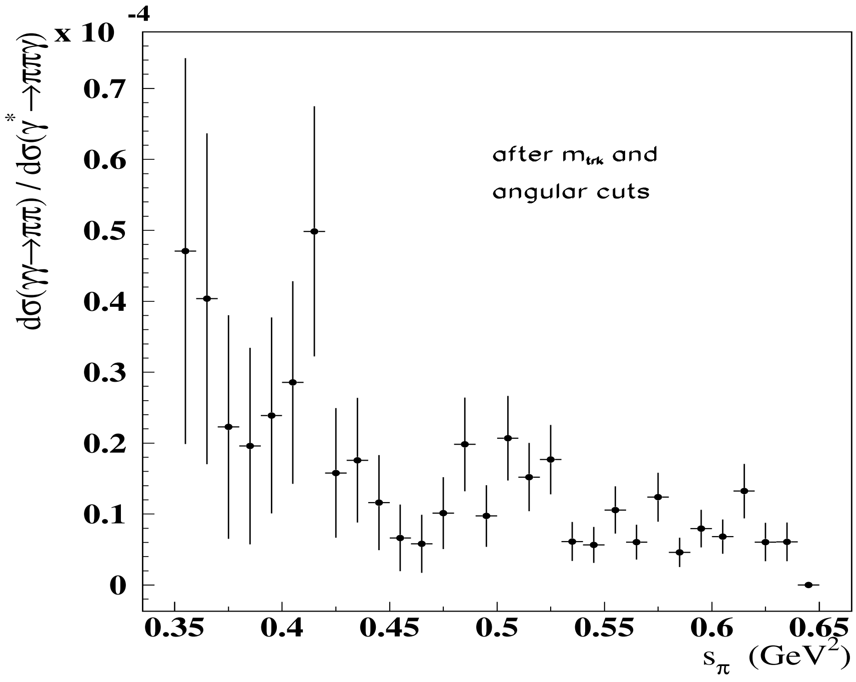

Figure 10: The ratio of the contribution of the photon photon fusion Feynman diagram to the process $e^+e^- \to e^+e^-\pi^+\pi^-$ with respect to the signal, after m_{trk} , θ_π and θ_Σ cuts.

shown in Fig. 10 and is found negligible. Concerning the contributions of either an initial state or a final state photon converting in an $e^+ e^-$ pair, shown in the middle and in the lower Feynman diagram of Fig. 9, we consider as the systematic error the result of $d\sigma_{ee\pi\pi}/d\sigma_{\pi\pi\gamma}$ evaluated in reference [23] and shown in Fig.4b) of that paper.

$e^+e^- \to \mu^+\mu^-\gamma$ with FSR at NLO

The uncertainty from FSR terms at NLO, not taken into account in the Monte Carlo code used for estimating the $\mu^+\mu^-\gamma$ yield, has been estimated multiplying the result of $d\sigma_{(ISR+FSR)@NLO}/d\sigma_{(ISR\ only)@NLO}$ evaluated in Fig.7c of Ref. [25] by the fraction of $\mu^+\mu^-\gamma$ events present in our observed spectrum. This result is shown in Fig. 11.

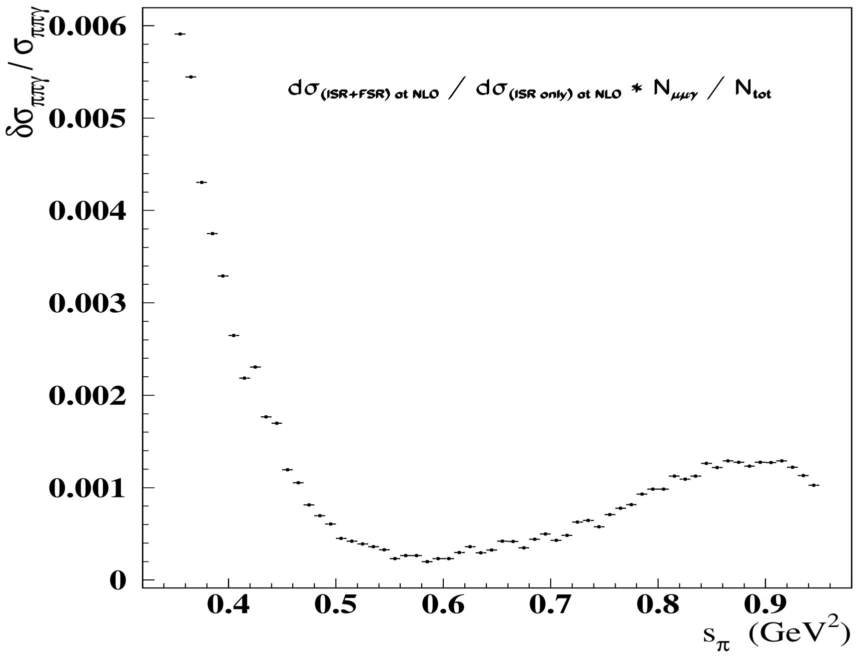

Figure 11: The relative systematic uncertainty in the measurement of the differential $\pi^+\pi^-\gamma$ cross section arising from not considering FSR terms at NLO.

4.2 Selection Efficiencies

This section is dedicated to the treatment of all efficiencies needed to extract $d\sigma(e^+e^- \to \pi^+\pi^-\gamma)/ds_\pi$. The combined total efficiency is $\sim 60\%$. A plot of it in bins of s_π can be found in Fig. 24.

4.2.1 Trigger and trigger veto

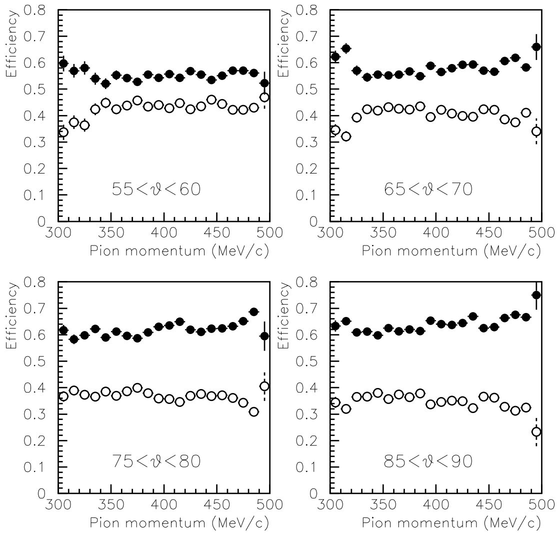

Figure 12: Probability of firing 1 (full circles) or 2 (empty circles) trigger sectors, as a function of pion momentum, for four different angular bins.

Events are selected in the $\pi^+\pi^-\gamma$ sample if they satisfy the *calorimeter trigger*, *i.e.* at least two *trigger sectors* with energy deposition above threshold must exist, provided they are not in the same end-cap (for details on the KLOE trigger see [20]). A second trigger condition, named *cosmic ray veto*, is applied to all events in order to reject online the large fraction of cosmic ray events which, otherwise, would fill up the available bandwidth. While the first request is rather efficient on signal events ($> 95\%$), the cosmic ray veto heavily effects $\pi^+\pi^-\gamma$ events, in particular at large values of s_π, since they mimic cosmic rays[3].

The trigger efficiency cannot be reliably obtained from Monte Carlo simulation, since it depends upon the details of the pion hadronic showers, so it must be derived from data. The method used to find the efficiency is explained in [26]. In short, a sample of events is selected in which one of the two tracks satisfies by itself the trigger condition, then the other track, the candidate track, is analyzed and the global efficiency is derived as specified below:

[3]The cosmic ray veto cuts on energy deposition only, and not on timing information which is not available at this stage.

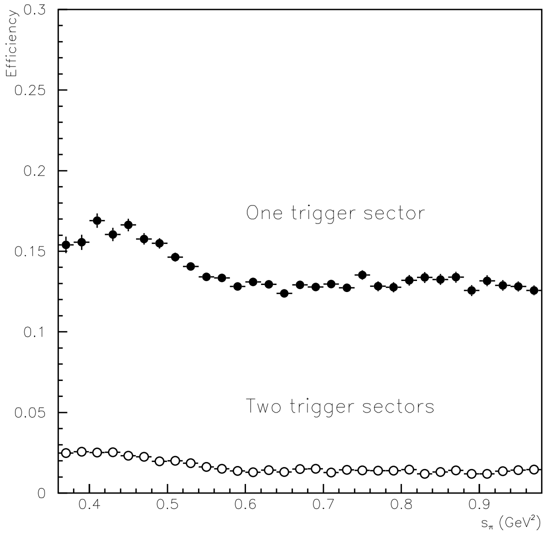

Figure 13: Probability that the *rest of the event*, excluding the two pion tracks, fires 1 or 2 trigger sectors.

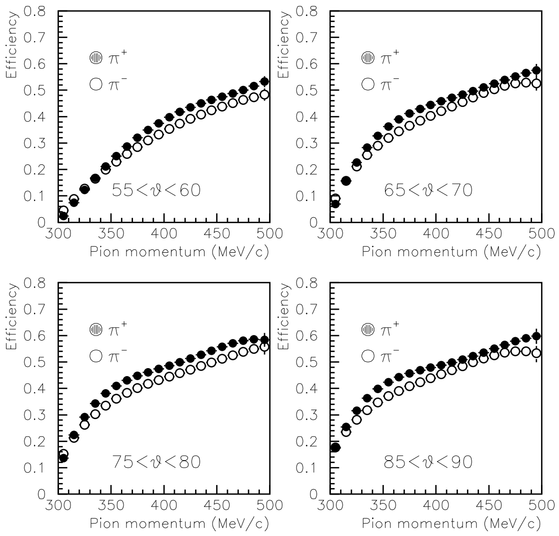

Figure 14: Probability that a π^+ or a π^- fires a cosmic ray veto sector, as a function of pion momentum, for different θ slices.

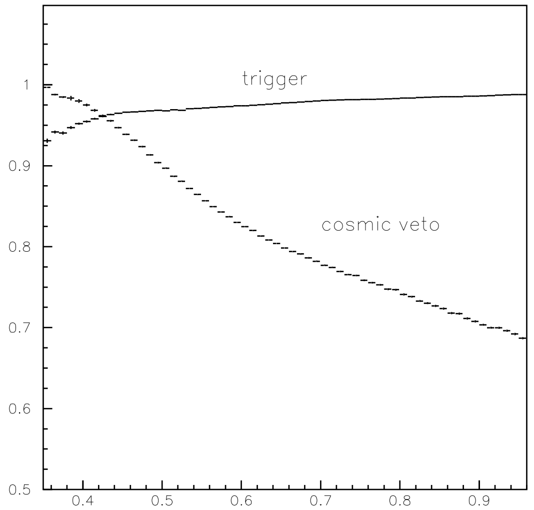

Figure 15: Trigger and cosmic ray veto efficiency. The total trigger efficiency is the product of the two.

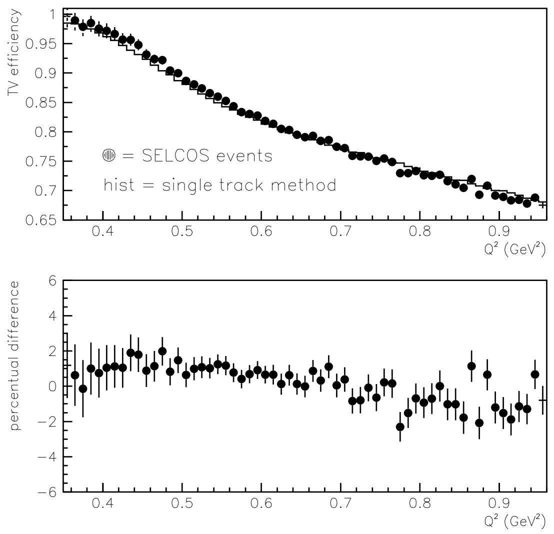

Figure 16: Efficiency on the cosmic veto trigger as evaluated with the single track method and using SELCOS events (see text).

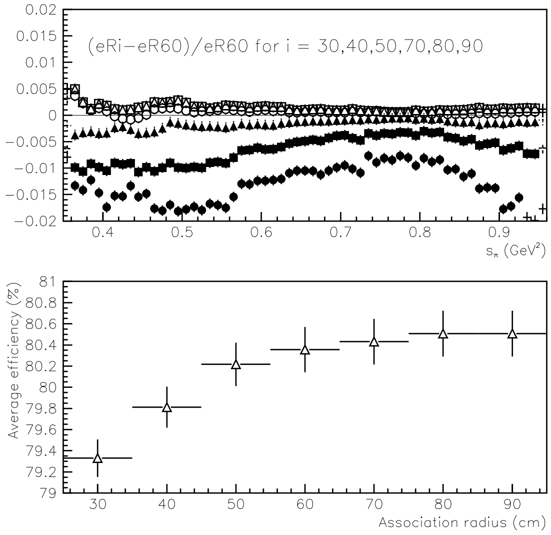

Figure 17: Efficiency as a function of the association radius.

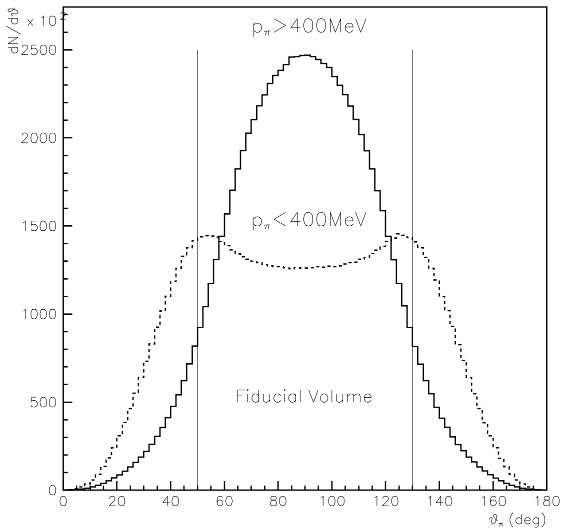

Figure 18: Pion angular distribution for two different momentum ranges. The high momentum tracks are preferentially emitted at large angles.

- the candidate track is extrapolated to the calorimeter[4] and associated to all clusters whose centroid lies in a sphere of 60cm from the extrapolation point;
- the clusters are associated to one or more trigger sectors using the information stored in the CTRG bank (*Cluster to TRiGger sector bank*);
- the probability that the track fires 0, 1 or 2 trigger sectors, as a function of its momentum and polar angle, is evaluated (see fig.12);
- the probability that a given event satisfies the trigger condition is evaluated by correctly combining the two track probabilities, where each probability depends upon the particular configuration of the event;
- finally, the trigger efficiency as a function of s_π is evaluated by generating with Monte Carlo the correct kinematics and by weighting each event with its probability.

The procedure described above, defined the *single track method*, assumes that the two tracks are independent in terms of probability for firing a trigger sector. This assumption is correct, provided the two tracks do not fall into the same trigger sector. Since the trigger sectors correspond to 15^0 in the ϕ angle, events in which the two tracks have $\Delta\phi < 15^o$ are always considered as inefficiencies, unless a track fires the trigger by itself. The fractions of events of this kind is smaller than 10^{-4}, therefore no appreciable bias is introduced with this cut. Another correction to the above procedure is necessary in order to take into account the probability that the *rest of the event* satisfies the trigger condition. This can happen if a fragment of a pion cluster, a secondary particle emitted by the small angle photon hitting the quadrupoles or a pile up event, fires a trigger sector. The probability for this to happen is sizeable, as shown in Fig. 13, and must be taken into account while evaluating the trigger efficiency. In particular, one can note that the probability that the rest of the event fires one or two trigger sectors is flat in s_π, down to 0.5 GeV^2, while it rises for low values of s_π, which corresponds to low momentum tracks. Low momentum tracks are on average more forward than the high momentum ones, as shown in Fig. 18. Pions which hit the ECAL at $\theta \sim 50^o$ can produce a secondary fragment that hits the End Cap calorimeter and produces a cluster far from the particle impinging point. In this case the cluster is associated to the *rest of the event* category.

An additional problem in the determination of the trigger efficiency is its possible correlation with the cosmic veto. In fact, at least in principle, events which are removed by the cosmic veto could have a different probability of firing the trigger than the events accepted. Since in this stage we need an unbiased effeciency, this possible effect must be corrected. This has been done by using the so called *SELCOS events*, which are a prescaled sample of the events identified by the trigger veto which are written in the output stream. The same prescale factor has been applied to the *normal* (non-SELCOS) events and the trigger efficiency has been evaluated using the global sample of *SELCOS* + prescaled non-*SELCOS* events, a sample unbiased from the point of view of the cosmic veto. The difference between evaluating the trigger efficiency using this unbiased sample and using the events of the *normal* data stream is 0.3%, a measurement of the correlation between the calorimeter trigger and the cosmic veto.

[4] The extrapolation method has been developed by Claudio Gatti and Tommaso Spadaro.

The efficiency of the cosmic veto must be evaluated with respect to the trigger efficiency, so it is evaluated on the events written in the *normal* data stream (*i.e.* non-SELCOS events) using a method which is totally similar to the one described before: the probability that a track fires a *trigger veto* sector is evaluated, as a function of momentum and polar angle (see Fig. 14) and then Monte Carlo kinematics for signal events is used to combine the single track probability as a function of its kinematical properties: momentum and polar angle. The single track method can be cross checked with data using the prescaled sample of events identified as cosmics (*SELCOS events*) and recorded to be analyzed offline. The cosmic veto efficiency can be evaluated as the number of signal events, in each s_π bin, divided by the same number plus the number of signal events identified as cosmics, weighted by the inverse of the prescale factor. To find the signal events in the prescaled *SELCOS* stream, all the analysis chain is run on this stream. The comparison between the single track method and the method based on prescaled events is shown in Fig. 16. It must be stressed the fact that this last method is correct only if the efficiency of the cosmic ray filter is independent from the efficiency of all the other modules. This is not necessarily true: for example requiring a track connected to a cluster which satisfies the pion identification procedure may be correlated with the probability of firing the cosmic veto. On top of this, the residual background from $e^+e^-\gamma$ and $\mu^+\mu^-\gamma$ events further modifies the efficiency evaluated with SELCOS events. For this reason, this method is not directly used to evaluate the efficiency of the cosmic veto trigger.

The final efficiencies, both for trigger and cosmic ray veto, are plotted in Fig. 15.

The systematical uncertainties of the method are dominated by the correct track-to-triggersector association. In particular, the choice of a given radius for the sphere which is used for the association can induce a modification in the efficiency, either because some secondary clusters produced by the impinging track are not associated to the track itself, or because clusters from the rest of the event or from pile up events are incorrectly associated to the track. To check this effect, we have varied the association radius from 30cm to 90cm, in steps of 10cm. The relative variation of trigger+cosmic ray veto efficiency, with respect to the default value of 60cm, is shown in Fig. 17, both integral and as a function of s_π. The plot shows that choosing a too small radius, of 30cm or 40cm, part of the secondary clusters may be lost and the efficiency underestimated. The systematic error on a_μ can be estimated from the plot to be 0.2%. The systematic error on the cross section has been evaluated by fitting the difference in the efficiency with respect to the curve obtained with $R = 50$cm. The resulting error is $\delta\epsilon_{TRG}(s_\pi) = \exp(0.43 - 4.9 s_\pi) + 0.08$ (expressed in percent). The result is very much the same if one uses $R = 90$cm as a comparing curve.

4.2.2 Track fitting procedure

The tracking efficiency has been evaluated selecting two control samples, $\pi^+\pi^-\pi^o$ and $\pi^+\pi^-$, identified without explicitely requiring the presence of one of the two tracks and then by checking if the track has been actually found by the track fit procedure. The two control samples are selected as follows:

- $\pi^+\pi^-\pi^o$

  1. two and only two prompt clusters with $E_{clu} > 30$ MeV and 29 cm/ns$\leq R_{clu}/t_{clu} \leq$

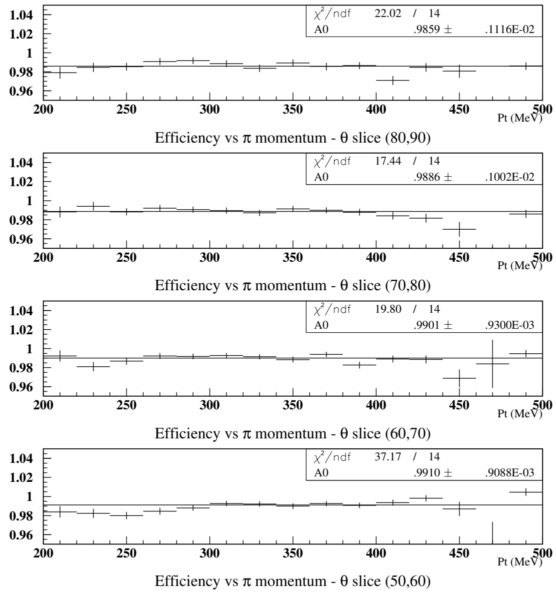

Figure 19: Ratio of tracking efficiencies as found by data and by Monte Carlo as a function of pion transverse momentum and for different slices in polar angle.

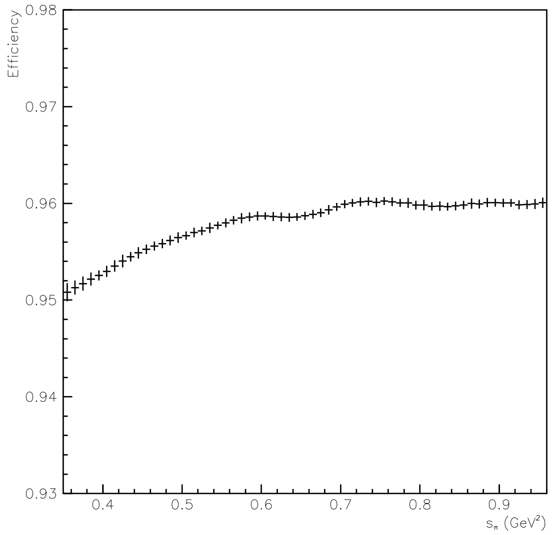

Figure 20: Tracking efficiency as a function of s_π.

32 cm/ns, where R_{clu} and t_{clu} are the position and the time of the cluster centroid with respect to beam crossing;

2. $|M_{\gamma\gamma} - m_{\pi^0}| < 20$ MeV, $M_{\gamma\gamma}$ being the invariant mass of the two clusters;
3. at least one track, that we call *tagging track*, associated to a cluster satisfying the pion identification procedure and whose backward extrapolation to the interaction point (*point of closest approach*) satisfies the following requirements: $\rho_{PCA} = \sqrt{x_{PCA}^2 + y_{PCA}^2} < 8$ cm and $|z_{PCA}| < 7$ cm;

- $\pi^+\pi^-$

1. one or two clusters in the central calorimeter with 5 ns $< t_{clu} <$ 8 ns;
2. at least one tagging track, satisfying the conditions of point 3 above, with the additional requirement, deriving from the two body decay kinematics, of 485 MeV $< |p_\pi| <$ 495 MeV.

The $\pi^+\pi^-\pi^0$ sample is rather clean, due to the tight constraint on the π^0 mass. However the momentum distribution of the charged pion is limited to 450 MeV. Pions from $\pi^+\pi^-$ events are used to study the efficiency in the high momentum region, but this sample needs a further cleanup, since the conditions are rather loose and allow for many background events to creep in. A particular kind of background events which could heavily affect the track resolution, are the so called *monotracks.* These events are protons, produced by the beam interactions with the pipe or with the material outside the beam pipe, which hit the calorimeter depositing all their energy in the first layer. These events can be identified by applying a cut on the number of calorimeter cells which form the cluster associated to the tagging track. The requirement is that the cluster has at least three cells above 7 MeV of deposited energy. This cut does not affect the track efficiency determination.

Then, for each control sample, the fraction of events having a candidate track with:

- opposite charge with respect to the tagging track;
- first hit in the drift chamber with a radius in the transverse plane $\rho_{FH} = \sqrt{x_{FH}^2 + y_{FH}^2} <$ 50 cm;
- point of closest approach to the beam line with $\rho_{PCA} = \sqrt{x_{PCA}^2 + y_{PCA}^2} < 8$ cm and $|z_{PCA}| < 7$ cm;

defines the tracking efficiency as a function of momentum and polar angle, $\epsilon_{trk}(p_{\pi^\pm}, \theta_{\pi^\pm}) \equiv \epsilon_{trk,\pm}$. Clearly the same cuts are also used in the signal selection as well as in the definition of the vertex efficiency (see Sec. 4.2.3). The single track efficiency as a function of p_π, for different slices of θ_π, has been compared with the one evaluated with Monte Carlo (Fig.19). The difference between the two efficiencies ranges from 99.1% to 98.6% and it is flat in momentum. For this reason the Monte Carlo efficiency has been scaled down by $(0.9910 + 0.9859)/2 = 0.9885$ and used to evaluate the track efficiency as a function of s_π. A systematic of $(0.9910 - 0.9859)/2 \sim 0.3\%$ is applied to the procedure. The resulting efficiency is shown in Fig. 20.

4.2.3 Vertex finder

The efficiency of the vertex finder algorithm has been evaluated with Monte Carlo and checked with a sample obtained from data. The data sample is defined by the following cuts:

- one prompt photon with 29 cm/ns $\leq L_{clu}/t_{clu} \leq$ 32 cm/ns and E_{clu} >20 MeV;
- two tracks with opposite charge, each with ρ_{FH} <50 cm, ρ_{PCA} <8 cm and $|z_{PCA}|$ <7 cm;
- at least on of the two tracks must be associated to a cluster satisfying the pion identification procedure;
- $\sin\theta_{12} < \sin 15^o$, where θ_{12} is the polar angle of the vector $\mathbf{p}_{12} = \mathbf{p}_1 + \mathbf{p}_2$, $\mathbf{p}_1$ and $\mathbf{p}_2$ being the momentum of the two tracks in the center of mass system (which means taking into account the small ϕ momentum);
- M_{12} >550 MeV, where the mass of the system is evaluated in the pion mass hypothesis for the two tracks.

These cuts select a sample of $\pi^+\pi^-\pi^0$ and $\pi^+\pi^-\gamma$, with some contamination from $\mu^+\mu^-\gamma$ and $e^+e^-\gamma$ events. The fraction of events with a vertex in the fiducial volume is evaluated as a function of s_π and plotted in Fig.21 for data and Monte Carlo. In the same figure the ratio of the two efficiencies is also shown. The Monte Carlo well represents the vertex efficiency. In order to evaluate a possible systematic effect on a_μ, we fit, in Fig.22, the ratio of the two efficiencies with two other functions: a straight line and two constant values in two different part of the spectrum. All of these fits agree well with the ratio. The difference in the a_μ integral is -0.2%, using hypothesis of Fig.22, upper, and -0.3%, using hypothesis of Fig.22, lower. We take a total systematics of ±0.3% due to the vertex fit procedure.

4.2.4 Offline reconstruction filter

During data taking, an offline filtering procedure tries to identify background events right after they have passed the calorimeter reconstruction. This procedure helps to save CPU time, since the rejected events do not enter the timeconsuming track fitting and pattern recognition algorithms. In order to evaluate the effect of this filter on the signal, a subsample of 16 pb^{-1} of the rejected events was recovered by reprocessing them. Since the filtering procedure is very sensitive to accidental clusters in the electromagnetic calorimeter, the unstable machine background conditions during the 2001 data taking made a parametrization of the filtering efficiency in terms of machine background necessary. The final efficiency ϵ^{final} was then evaluated according to the following formula:

$$\epsilon^{final}(s_\pi) = \frac{\sum_i^{runs}\left(L_i \cdot k_i(\mathrm{bclde}) \cdot \epsilon^{\mathrm{repr}}(\mathrm{s}_\pi)\right)}{L_{tot}} \tag{4.2}$$

The sum runs over all the data runs used in the analysis, L_i is the integrated luminosity for each run, L_{tot} is the total integrated luminosity of 141.4 pb^{-1}, $\epsilon^{\mathrm{repr}}(s_\pi)$ is the efficiency

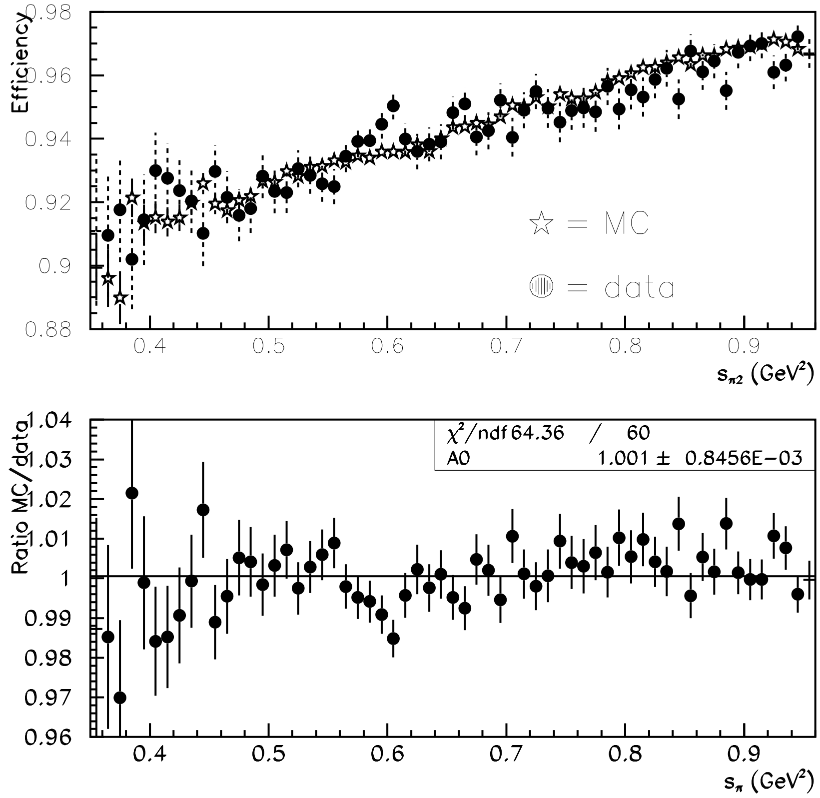

Figure 21: Upper: vertex efficiency, comparison data Monte Carlo. Lower: ratio between the two efficiencies and fit with a constant.

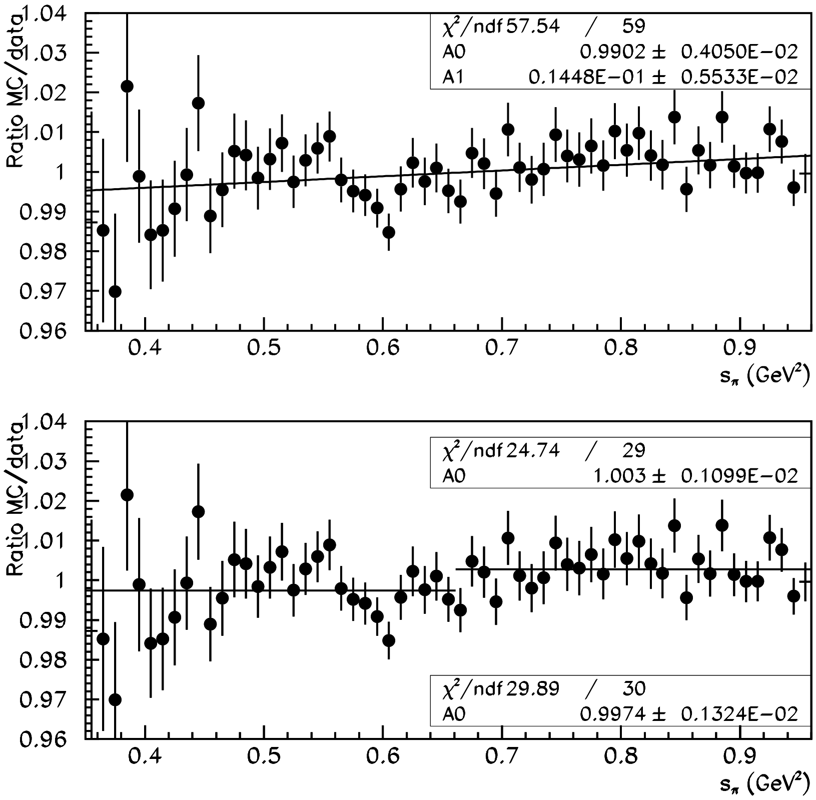

Figure 22: Ratio between the vertex efficiency evaluated with Monte Carlo and with data fit with a straight line (upper plot) and with two constants (lower plot).

evaluated from the subsample of reprocessed runs and finally $k_i(bclde)$ is the parametrization factor which takes into account the dependance of the efficiency on the background conditions for each single run. For the analysis, $\epsilon^{\mathrm{repr}}(s_\pi)$ has been evaluated after all other analysis signal selection items, in order to be sure to get the efficiency for a clean sample of signal events.[5] For the parametrization of background conditions, the quantity *bclde* is used which averages for each run the remaining energy deposit in the calorimeter for Bhabha events after attributing the two most energetic calorimeter clusters to the Bhabha event itself. Since for clean Bhabha events no additional calorimeter energy apart from the two Bhabha tracks is expected, a high value of *bclde* indicates a high value of background in the corresponding run. Fig. 23 shows the linear dependance found between the s_π-averaged FILFO efficiency and *bclde*. Eq. 4.2 then ensures that every run contributes to the final efficiency according to its luminosity and the background conditions which were present at the time when the data of the run was taken. The final efficiency averaged in s_π was found to be about 96.6%. The errors of the parametrization introduce a 0.6% systematic error on the final efficiency. This error is independent from s_π. A more detailed discussion about the evaluation of the offline filter efficiency and the systematic error can be found in [27].

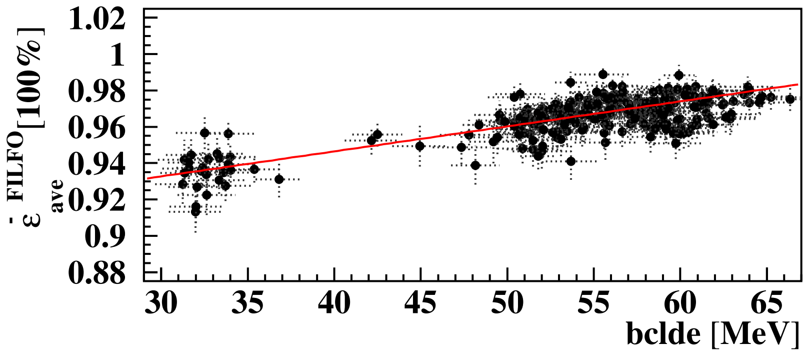

Figure 23: The efficiency of FILFO averaged in s_π is plotted for each reprocessed run against the variable *bclde* explained in the text. The straight line corresponds to a linear fit which has a $\chi^2/ndof = 255.4/250$ and is used to obtain the parametrization factor $k_i(bclde)$ in Eq. 4.2.

4.2.5 Pion identification

The efficiency for the likelihood cut has been evaluated by selecting $\pi^+\pi^-\gamma$ events on the basis of one track and examining the distribution in ζ for the other one. In the analysis, only one track is required to satisfy the likelihood cut, for which the efficiency is $> 99.9\%$.

[5]This is possible if in the determination of all other analysis items the offline filter was not active or does not play a role.

Therefore, no correction for the pion ID inefficiency needs to be applied; the contribution to the systematic error is taken to be 0.1%.

4.2.6 Particle mass

The efficiency of the m_{trk} cut is obtained as a by-product of the residual background evaluation; the result of the fit provides the efficiency in each s_π bin. However, this efficiency depends upon the way the Monte Carlo treats multi-photon processes. The m_{trk} efficiency has been obtained with our reference Monte Carlo, which uses PHOKHARA. To check the efficiency determination we have compared PHOKHARA with BABAYAGA, the same generator used in the luminosity measurement. In this generator, ISR is treated using the parton shower approach. The resulting value for the m_{trk} efficiency differs from that evaluated with PHOKHARA by 0.2%. The additional contribution to the efficiency, which is the contemporary emission of an ISR and a FSR photon, described in PHOKHARA, is discussed in section 6.1.

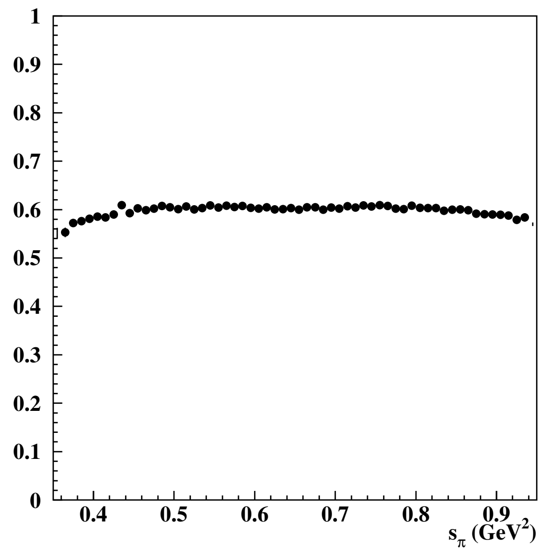

Figure 24: Plot for the total efficiency, combined from all individual efficiencies. The full scale maximum of the y-axis represents 100 %.

4.3 Unfolding the mass resolution

In order to obtain $d\sigma_{\pi\pi\gamma}/ds_\pi$ as a function of the true value of s_π, we unfold the mass resolution from the measured s_π distribution. The measured value of $s_{\pi,\mathrm{obs}}$ is related to the true value by a resolution matrix $\mathbf{G}(s_{\pi,\mathrm{true}} - s_{\pi,\mathrm{obs}}|s_{\pi,\mathrm{true}})$. This matrix has been generated by Monte Carlo simulation. At a bin width of 0.01 GeV^2, the resolution matrix is nearly diagonal with 75% of the events in the diagonal, 11% in each of the first once-off-diagonal elements and only 3% in the remaining elements. The matrix is graphically illustrated in Fig. 25, left. Unfolding of the spectrum is obtained by using GURU [29], an unfolding program based on singular value decomposition (SVD).

In the upper plot of Fig. 25, right, the relative difference between the reconstructed and the generated spectra is shown without the application of the unfolding procedure (solid line), and using simple matrix inversion $\mathbf{G}^{-1}$ (points), for the MC sample. In the lower plot the results obtained by GURU are compared for two different values of the regularization parameter (τ_{10} and τ_{40}), which show a clear improvement of the result, respect to the previous plot. τ_{10} is the value of the regularization parameter which is chosen in the unfolding procedure [30].

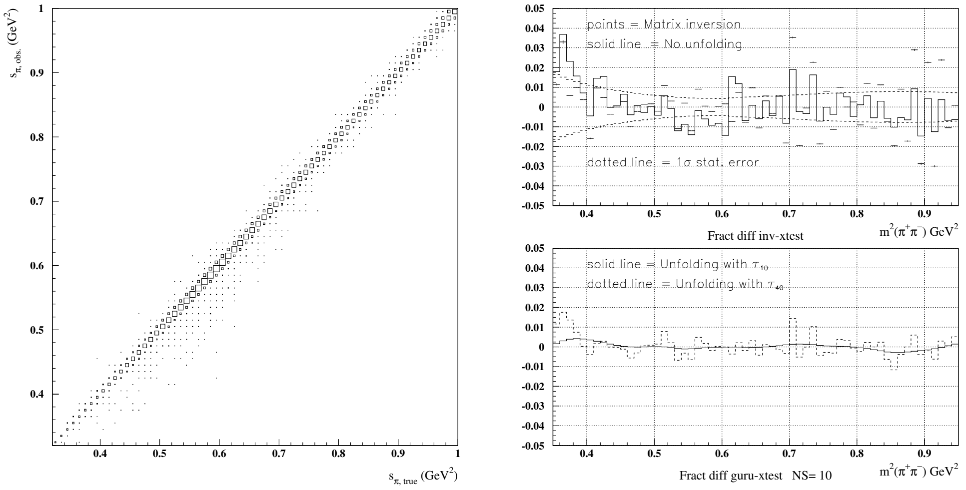

Figure 25: Left: smearing matrix representing the correlation between generated ($s_{\pi,\text{true}}$) and reconstructed ($s_{\pi,\text{obs.}}$) values for s_π; the high precision of the DC results in an almost diagonal matrix. Right: fractional difference between reconstructed and generated spectrum without unfolding (*up*, *solid line*), with matrix inversion (*up*, *points*) and unfolding with GURU (*down*, for two different values of the regularization parameter [30]). In the upper plot the one σ statistical fluctuation of the sample is also shown (dashed line).

The effect of the unfolding procedure on data depends both on the accuracy in the evaluation of the response matrix and on the proper choice of the regularization parameter. These items will be discussed in the following.

4.3.1 Systematics due to reconstruction effects

The effect of a residual resolution difference between data reconstruction and Monte Carlo simulation in the unfolding procedure has been studied using PHOKHARA3 events reconstructed with version 18 of the detector simulation program.

The simulated momenta of the pions have been corrected to recover the discrepancy between data and Monte Carlo visible in the trackmass distribution (Fig. 26a). On this

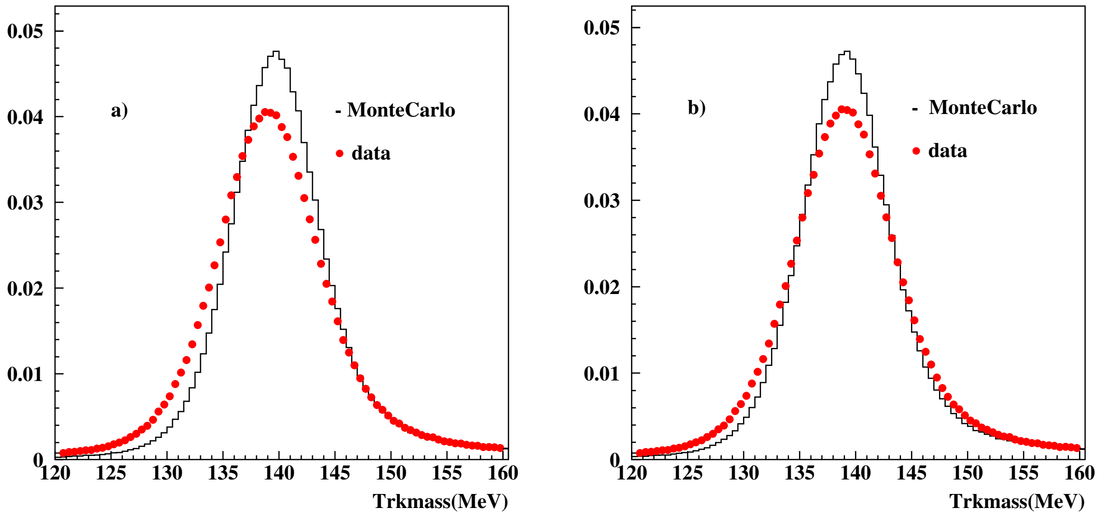

Figure 26: a) Data-Monte Carlo comparison before any momentum correction; b) data-Monte Carlo comparison after correcting the pion momenta as in [31].

purpose we have used the momentum corrections already applied in the analysis of the process $\phi \to \pi^+\pi^-\pi^0$ [31] [6]. These corrections move the central value of the simulated trackmass distribution to the experimental value, as shown in Fig. 26b. A small discrepancy is still visible: Fig. 27a shows the difference between simulated and experimental mean value of the trackmass distribution as a function of the invariant mass squared of the two pion system, for $\theta_\pi < 90^o$ and $\theta_\pi > 90^o$. In the latter case, where the discrepancy is larger, a fit to the distribution is performed and the fit function is used to correct the pion momenta. The result is shown in Fig. 27b. The width of the simulated trackmass distributions is adjusted to match data applying a gaussian smearing to the Monte Carlo momenta. Fig. 28 shows the final comparison of Monte Carlo and data. As a consequence of the momentum correction, also the simulated θ_Σ distribution matches better the experimental one, as visible in Fig. 29, showing the data-Monte Carlo comparisons before, a), and after, b), correcting the pion momenta. Fig. 30 shows the total effect of these corrections on the Q^2 spectrum, including all changes to the acceptance, to the trackmass cut efficiency and to the smearing matrix. The systematic error attached to these corrections, evaluated by slightly modifying width and mean value of the Monte Carlo trackmass distribution, has been found to be on the permille level and is therefore inside the error of the unfolding procedure. The corrections have been considered in the previous section on the Monte Carlo test of the unfolding.

4.3.2 Systematic error due to the regularization parameter

The error introduced by the unfolding procedure can be estimated by Monte Carlo using a "test" distribution close to the unfolded one and by comparing the output of the unfolding procedure with the "test" distribution.

[6] Since sagitta effects are simulated in Monte Carlo, any dependence of the corrections on the azimuthal angle has been neglected.

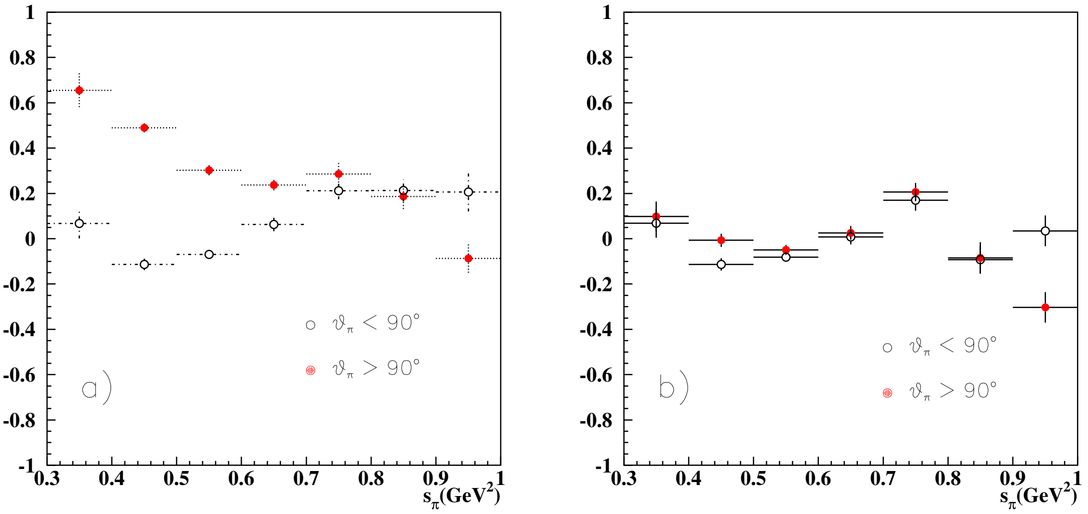

Figure 27: a) Difference in MeV between simulated and experimental mean value of the trackmass distribution as a function of s_π for $\theta_\pi < 90^o$ and $\theta_\pi > 90^o$; b) corrected difference.

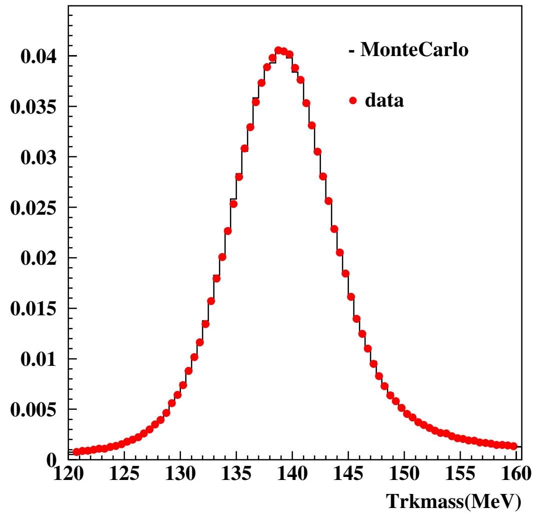

Figure 28: Corrected Monte Carlo trackmass distribution compared to the experimental one: a gaussian smearing has been applied to the pion momenta to reproduce the experimental width.

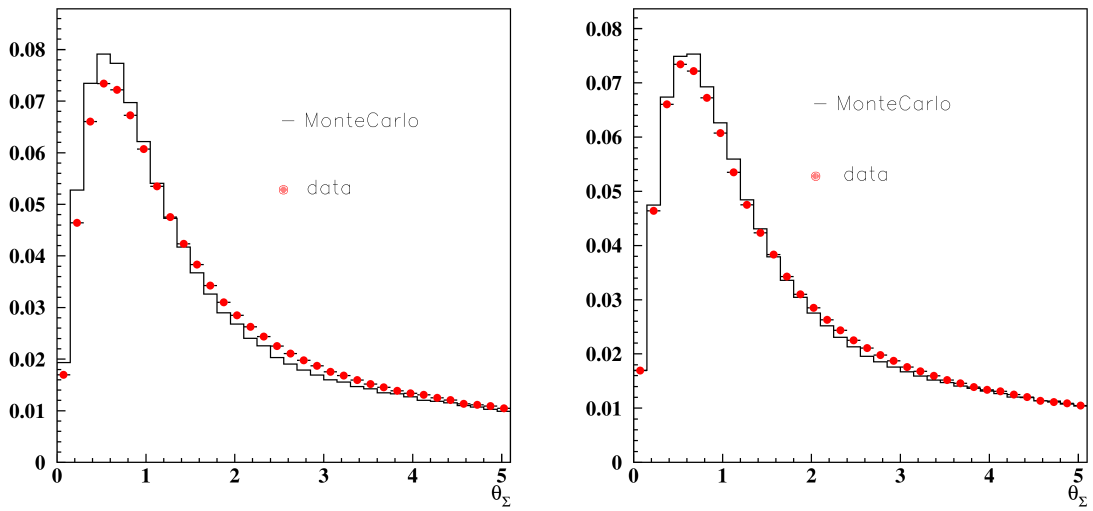

Figure 29: Simulated θ_Σ distribution compared to the experimental one, a) before and b) after correcting the pion momenta.

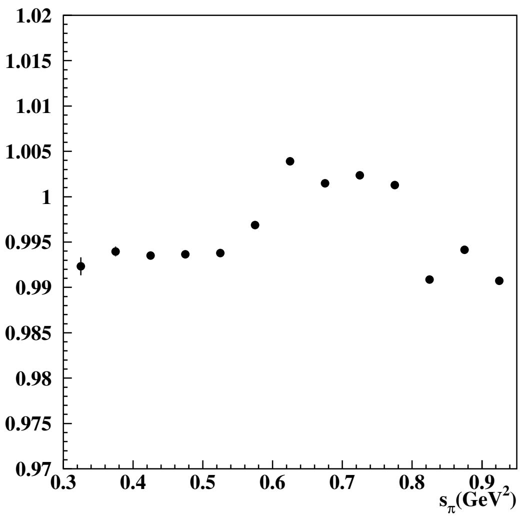

Figure 30: Total effect of the pion momentum corrections on the Q^2 spectrum, including all changes to the acceptance, to the trackmass cut efficiency and to the smearing matrix.

We consider three different distributions which are close to the unfolded spectrum, since they were chosen to reproduce the KLOE observed spectrum, once the smearing matrix, the selection chain and the background subtraction were applied, as shown in Fig. 31.

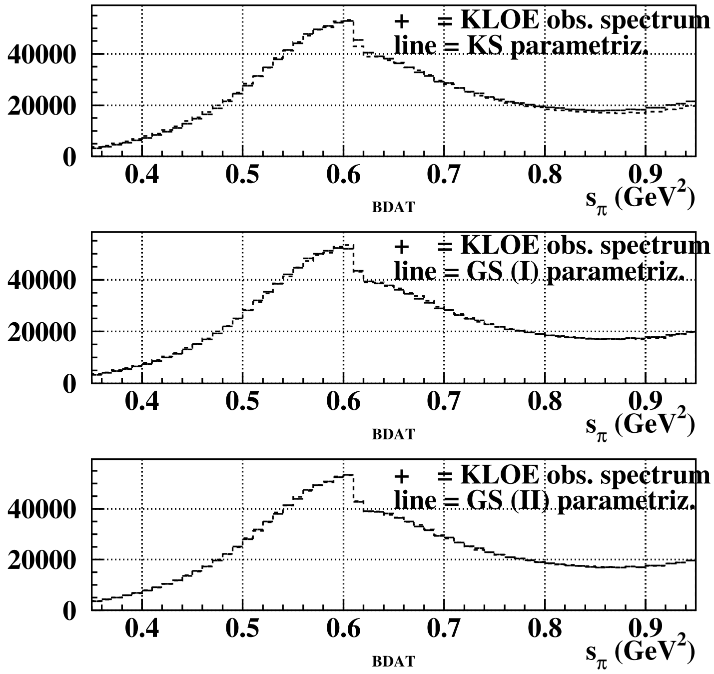

Figure 31: Comparison between the "test" distibutions (*line*) and the observed KLOE spectrum (*dots*), after background subtraction. The distribution in the top of the figure was based on the Kühn- Santamaria (KS) parametrization of the pion form factor, while the distributions in the middle and bottom of the figure were based on a Gounari-Sakurai (GS) parametrization. These distributions were corrected for smearing effects and selection efficiencies, in order to compare with the KLOE observed spectrum.

The error due to the unfolding procedure was then estimated by constructing a toy Monte Carlo using as "test" distributions these spectra, and applying the unfolding procedure to the "smeared" spectra. The same choice of the regularization parameter of the data spectrum (τ_{10}) was applied. Fig. 32 shows the relative difference of the unfolded spectra with respect to each "test" distribution: as it can be seen the systematic effect (if any) for each distribution is very limited to the region around the ρ peak. This allowed us to give an estimate of the error introduced by the unfolding procedure, which was taken as average of the differences (in absolute value) in the region $0.58 \leq s_\pi \leq 0.66$, and is given in Tab. 5. These errors must be considered as diagonal, correlated systematic errors, and translate 0.2% systematic uncertainty on a_μ.

As final remark, the presence of the regularization term affects the covariance matrix

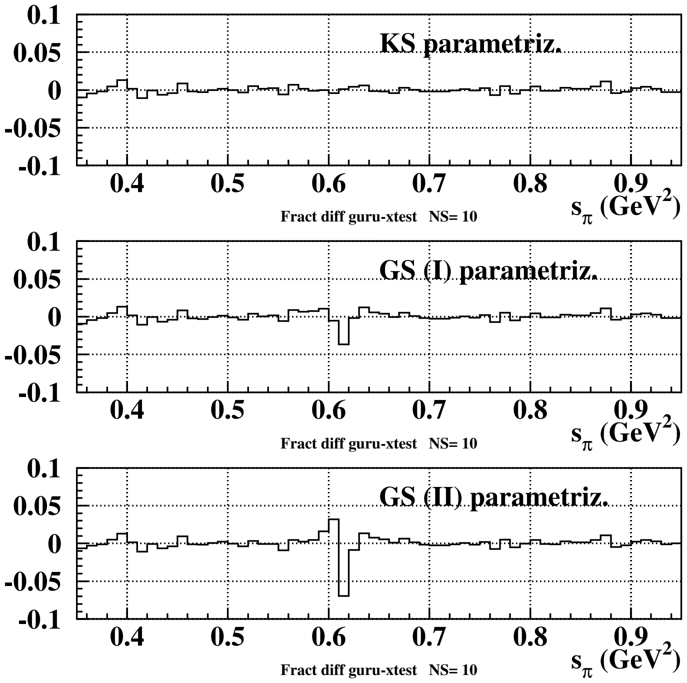

Figure 32: Relative difference between the unfolded spectra and the "test" distribution. These differences give an estimate of the error due to the unfolding, which, as can be seen, is limited to the region around the ρ.

of the unfolded spetrum, as discussed in [30]. The full covariance matrix X^τ must be used for a correct error propagation involving the unfolded vector (for example in the evaluation of the statistical error on a_μ). The unfolding procedure is necessary in order to provide a table of data points at meaningful values of s_π. However, the procedure itself introduces additional systematic uncertainties because of the numerical instability of the problem. For the comparison of the data with a specific theoretical prediction, one does not need to unfold, since the fit of the observed spectrum using a convolution of the theoretical curve with the detector response matrix is a well defined and stable procedure (as done in ALEPH, see for example [32]). This is the suggested method, since it avoids complications related to the presence of the cut-off τ [33].

4.4 Acceptance

After correcting for the mentioned efficiencies (and unfolding), the $\pi^+\pi^-\gamma$ spectrum is still limited to the region $50^o < \theta_\pi < 130^o$, $\theta_\Sigma < 15^o$ or $\theta_\Sigma > 165$, $p_t > 160\,MeV$, $p_z > 90\,MeV$. In order to correct for the cuts on momentum and polar angle of the pions, an (acceptance) correction has been applied using PHOKHARA. The systematic error of 0.3% on the acceptance fraction has been estimated by a comparison of data and Monte

Carlo distributions.

5 Luminosity measurement

The integrated luminosity is measured with the KLOE detector itself using (very) large angle Bhabha (VLAB) events. The effective Bhabha cross section at large angles ($55^o < \theta_{+,-} < 125^o$) is about 430 nb. This cross section is large enough so that the statistical error on the luminosity measurement is negligible. The number of VLAB candidates, N_{VLAB}, is counted and normalized to the effective Bhabha cross section σ^{MC}_{VLAB}, obtained by Monte Carlo. The small relative amount of residual background δ_{Bkg} (see below) has been estimated directly from data and properly subtracted.

$$\int \mathcal{L}dt = \frac{N_{VLAB}(\theta_i)}{\sigma^{MC}_{VLAB}(\theta_i)} \cdot (1 - \delta_{Bkg}) \tag{5.1}$$

5.1 Theoretical Event Generators

The precision of this measurement depends on the correct inclusion of higher order terms in computing the Bhabha cross section. We use the theoretical Bhabha event generator BABAYAGA [36] which has been explicitly developed for DAΦNE. QED radiative correction are taken into account in the framework of the parton shower method. The quoted precision of the BABAYAGA generator is 0.5%. The result for the effective Bhabha cross section has been compared with BHAGENF [34] [35]) - a full order α event generator. We find agreement to better than 0.2%. Most recently a systematic and more general comparison of all available Bhabha events generators in the 1GeV range has been performed together with the authors of BABAYAGA. On this occasion BABAYAGA has been compared with two further generators: BHWIDE [37] and NSK [38], both using the structure function technique. NSK and BHWIDE are giving somewhat lower cross sections with respect to BABAYAGA; the difference is 0.4% in the case of NSK and 0.7% in the case of BHWIDE.

We conclude that there is reasonable agreement between the several available event generators and we take the theory error of BABAYAGA (i.e. 0.5%) as the theoretical uncertainty of the VLAB cross section. We have also checked the correct treatment of vacuum polarization (leptonic and hadronic) in BABAYAGA, both for the s-channel and the t-channel.

5.2 Experimental Precision

The effective cross section σ^{MC}_{VLAB} is calculated after having implemented the theoretical event generator BABAYAGA (and also BHAGENF) in the KLOE detector simulation environment, i.e. smearing effects due to the limited detector resolution are taken into account. From the experimental point of view the precision of the luminosity measurement is given by the precision with which the detector simulation is reproducing the relevant efficiencies and kinematical distributions. It is therefore important to choose selection cuts which are well simulated by the KLOE Monte Carlo program. In case of differences a correction has to be applied. We report in the following on the individual selection cuts and the corresponding analysis items:

- The acceptance region for the electron and positron polar angle ($55^o < \theta_{+,-} < 125^o$) is measured by the EmC clusters produced by these tracks. The cluster efficiency is measured with a sample of Bhabha events, which are selected without requiring any calorimetric information, using only the momenta and position measurement of the drift chamber. The probability for two tracks (with momenta > 400MeV, see below) to produce two clusters in the EmC has been found to be 99.6%, where a large part of the inefficiency (0.23%) is due to a noisy EmC-channel for which we have to apply a correction. The inefficiency due to this noisy channel has been checked to be stable throughout the 2001 data set.

- The energy measurement ($E_{+,-} > 400$ MeV) is performed by the high resolution drift chamber. We require both tracks to have a momentum above this cutoff value. The tracking efficiency is measured by selecting events with two high-energetic EmC-clusters at large polar angles and for which at least one high momentum track coming from the interaction point exists. Taking these requirements we are searching for a second track with opposite charge, momentum > 300MeV and some further topological requirements. Thus a tracking efficiency for VLAB-events of 99.8% has been found, which is in excellent agreement with the detector simulation prediction.

- The trigger inefficiency for VLAB-events is negligible. There has been found however a significant loss of events due to the cosmic ray veto. The effect is overestimated by Monte Carlo which predicts a value of 1.0%, while we find from data an inefficiency of only 0.5% by looking at the prescaled cosmic-ray events. We take into acoount this difference by correcting the effective VLAB cross section, see Tab 1.

- Background from $\mu^+\mu^-(\gamma)$, $\pi^+\pi^-(\gamma)$ and $\pi^+\pi^-\pi^0$ events is suppressed by the VLAB event selection to a level of 0.5% and is subtracted. This residual background is measured by looking at the trackmass distribution. Events of the kind $\mu^+\mu^-(\gamma)$, $\pi^+\pi^-(\gamma)$ are peaked at $m_{trk} = m_\mu$ and $m_{trk} = m_\pi$ respectively while $\pi^+\pi^-\pi^0$ events are populated at $m_{trk} > m_\pi$. In order to obtain the exact amount of background these peaks have to be separated from the huge tail of signal VLAB events which is reaching into the trackmass region of interest. This is done by extrapolating the Bhabha tail into the region $m_{trk} > 100$ MeV and by counting the number of events exceeding the tail. In a second independent approach the pion ID function has been applied under the pion hypothesis which efficiently rejects Bhabha events and selects the background channels. Both methods give very similar results and a conservative uncertainty for the background evaluation of 0.1% is assumed.

- We obtain excellent agreement between the experimental distributions ($\theta_{+,-}$, $E_{+,-}$) and those obtained from Monte Carlo simulations, see Fig. 33. A small correction (0.2%) has to be applied due to event losses at the borders of the polar angle distribution.

- The VLAB cross section is calculated run-by-run in order to account for fluctuations in the center-of-mass energy of the machine. We also apply efficiency corrections on a run-by-run basis in order to correct for drifts in the EmC calibration. The overall size of these corrections is very small ($< 0.2\%$). The final result for the integrated luminosity after these run-by-run corrections does not change with respect to the uncorrected result due to averaging effects.

The list of all analysis items related to the luminosity measurement together with the individual corrections and uncertainties is shown in Tab. 1. We assign a total systematic error for the luminosity measurement of $\delta\mathcal{L} = 0.5\%_{\text{th}} \oplus 0.3\%_{\text{exp}}$. A cross check of the VLAB luminosity measurement with an independent $e^+e^- \to \gamma\gamma(\gamma)$ counter, which shows agreement to within 0.2%, confirms this precision.

Analysis items Luminosity	Correction	Uncertainty
Acceptance	-0.2%	0.2 %
Knowledge W		0.1 %
Background	+0.5%	0.1 %
Tracking Efficiency		0.1 %
EmC Cluster Efficiency	-0.2%	0.1 %
EmC Calibration Drifts		0.1 %
Cosmic-Ray Veto	+0.5%	0.1 %
Total exp systematics	+0.6%	0.3 %

Table 1: List of systematic effects for the luminosity measurement. The corrections are due to a difference between data and Monte Carlo for the individual analysis items.

6 Radiative corrections

The precise measurement of the hadronic cross sections needs a careful treatment of radiative corrections. Apart from initial state radiation, which has been discussed in Sec. 1.2, final state radiation and vacuum polarizaton effects have to be correctly taken into account.

6.1 Final State Radiation (FSR)

6.1.1 LO-FSR versus NLO-FSR

$\pi^+\pi^-\gamma$ events in which a photon is radiated from the pion tracks (Final State Radiation, FSR) are indistinguishable on an event-by-event basis from events in which pure Initial State Radiation (ISR) is present. We distinguish in the following between LO-FSR events and NLO-FSR events, see Fig. 34 for illustration. In LO-FSR events no ISR-photon is present and hence the invariant mass of the off-mass-shell photon, s_{γ^*}, is not lowered with respect to the center of mass energy provided by the machine: $s_{\gamma^*} = m_\phi^2$. Those events have to be considered as a background to our ISR-approach, since we want to measure the coupling of the off-mass-shell photon to pions for values $s_{\gamma^*} < m_\phi^2$. In NLO-FSR events a photon from ISR *and* from FSR is emitted simultaneously and the virtual photon's invariant mass is lowered but does actually not coincide with the two-pions invariant mass s_π in the case of real final state photon emission: $s_\pi(NLO - FSR) < s_{\gamma^*}(NLO - FSR)$. The consequence of this will be discussed later in this section. Please notice that when we

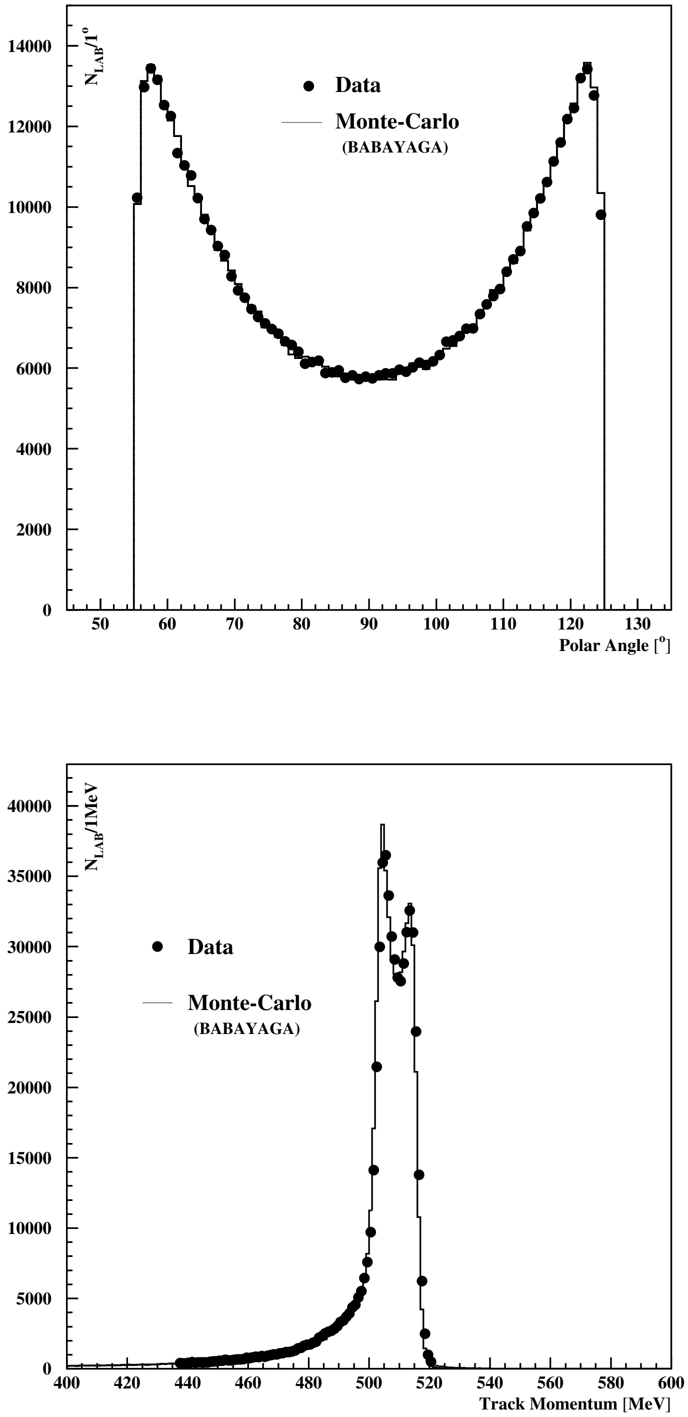

Figure 33: Comparison data-Monte Carlo of the $\theta_{+,-}$ (up) and $E_{+,-}$ (down) distributions for the Bhabha events selected at large angle as described in the text

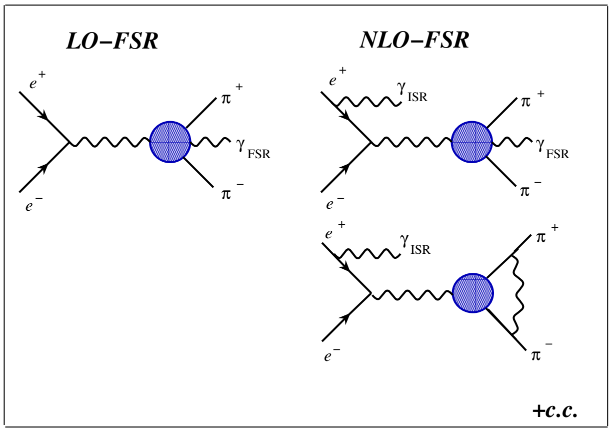

Figure 34: We distinguish between LO-FSR events and NLO-FSR events. While LO-FSR events are a background to our measurement, NLO-FSR events should be included in our selection (see text for further details).

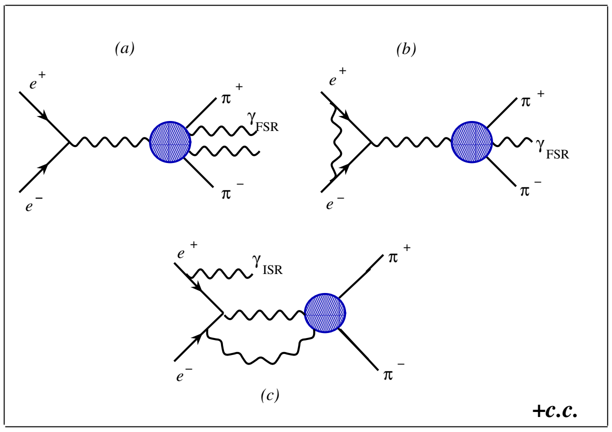

Figure 35: Contributions to $e^+e^- \rightarrow \pi^+\pi^-\gamma(\gamma)$ not simulated in PHOKHARA. See Ref. [11, 12, 25] for further details.

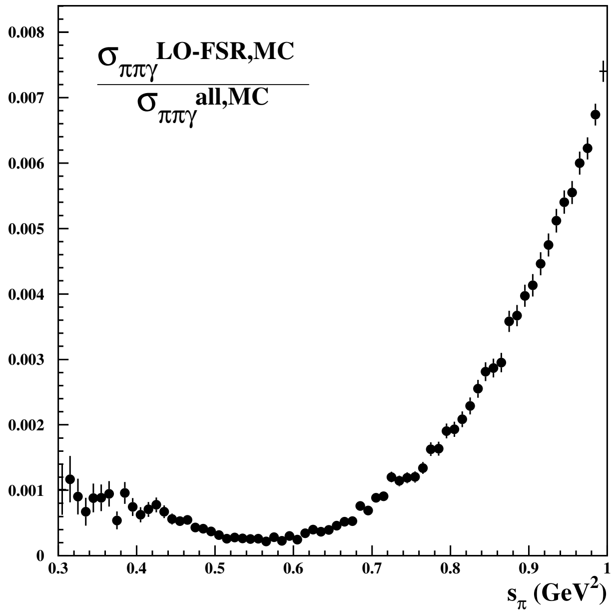

Figure 36: Plotted is the relative contribution of LO-FSR events (see Fig. 34, left) to the $\pi^+\pi^-\gamma$ cross section for the selection cuts chosen in our analysis. The cross section $\sigma_{\pi\pi\gamma}^{all,MC}$ contains the full NLO-ISR + LO-FSR + NLO-FSR - contributions. As can be seen from the plot the LO-FSR contribution is well below 1% over the entire energy range. The Monte-Carlo event generator PHOKHARA has been used for this plot.

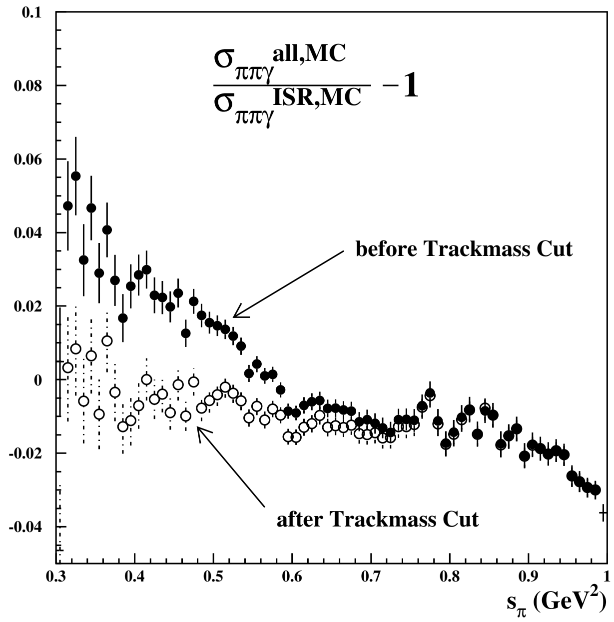

Figure 37: Plotted is the relative contribution of NLO-FSR events (see Fig. 34, right) before and after the cut on trackmass as predicted by PHOKHARA. The relatively high contribution at small values of s_π can be explained by those events in which ISR lowers the invariant mass of the two-pion-system to the ρ mass from which additional FSR is emitted. The trackmass cut considerably rejects these kind of events.

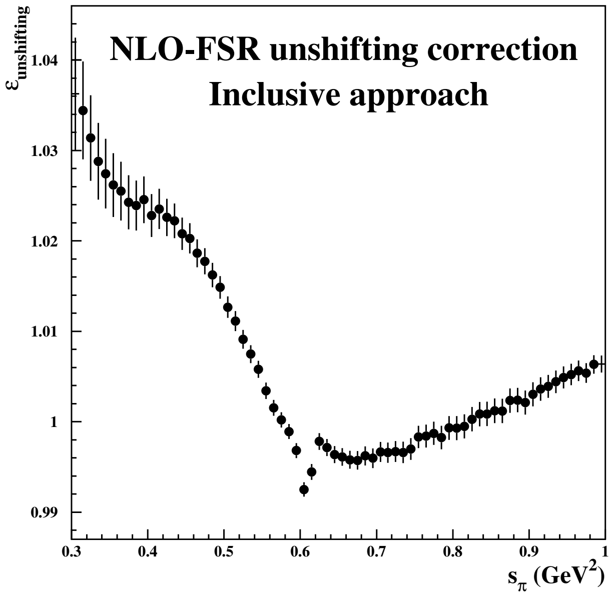

Figure 38: Unshifting function which has to be applied to data for the inclusive approach for FSR-corrections. This function corrects for a difference in the $d\sigma_{\pi\pi\gamma}/ds_\pi$ and the $d\sigma_{\pi\pi\gamma}/ds_{\gamma^*}$ spectra due to NLO-FSR events (see text for further explanation). The Monte Carlo event generator PHOKHARA has been used to obtain the correction function.

refer in the following to LO-FSR and NLO-FSR events, we refer *only* to the left and the two right graphs displayed in Fig. 34. Events in which two photons are emitted from the final state pions (Fig. 35, a), which also contribute to the full NLO-FSR correction - are not simulated in the current version of PHOKHARA and are considered to be negliglible for the following discussion (see also Ref. [11]). Also not considered are events with one real FSR photon and a virtual photon between the initial electron and positron legs (Fig. 35, b). In Ref. [25] it is shown that this contribution is negligible.

It is now commonly accepted that the cross section $e^+e^- \to \pi^+\pi^-$, which can be extracted from our $\pi^+\pi^-\gamma$ measurement using Eq. 1.2, and which has to be used in the dispersion relation to obtain $a_\mu^{\rm hadr}$, must be inclusive with respect to FSR (see Ref. [6] for details). The radiator function H does only describe the ISR part of the radiative corrections, and therefore NLO-FSR events in the cross section $e^+e^- \to \pi^+\pi^-\gamma$ correspond to the desired LO-FSR in the cross section $e^+e^- \to \pi^+\pi^-$ after the division by H. This assumes factorization though, i.e. the assumption that the ISR process and FSR process are decoupled. Contributions like the one from diagram (c) in Fig. 35 in which rather than only one virtual photon a second photon is connecting the electron/positron system with the pionic system are in contradiction with the factorization ansatz. We again assume that these contributions are negligible and we will come back to this issue at the end of the chapter. We conclude that it is important to subtract as much as possible LO-FSR events, while the relative contribution of NLO-FSR events needs to be known with a high level of precision.

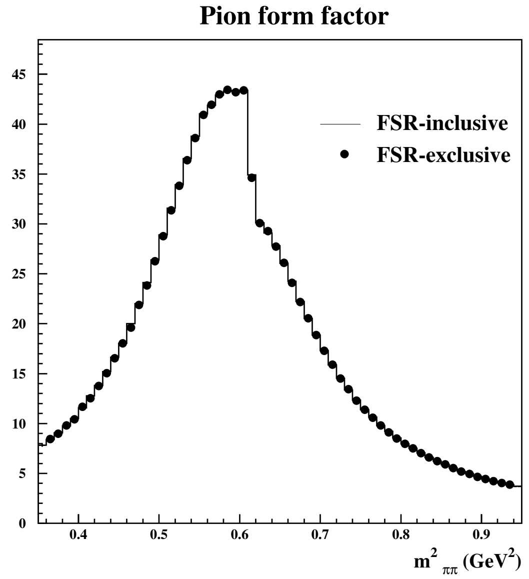

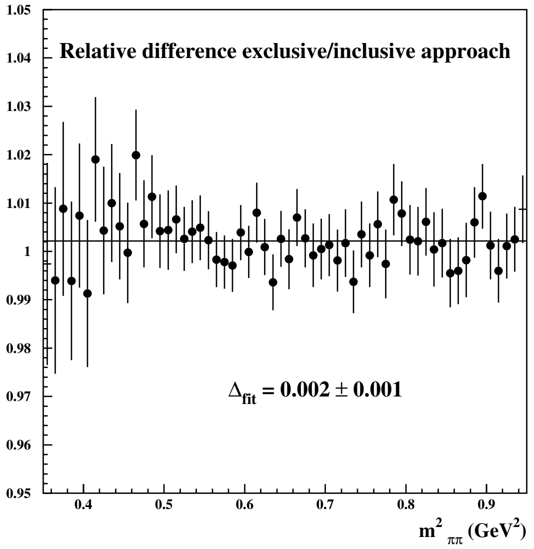

Figure 39: FSR corrections have been performed with two complementary approaches. In the first apprach the analysis is performed for a fictitious pure ISR cross section (exclusive approach) and at the end the full FSR-contribution to the cross section $\sigma(e^+e^- \to \pi^+\pi^-)$ is added. In the second approach the LO-FSR and NLO-FSR contribution is simulated by PHOKHARA and the analysis is performed inclusively with respect to these FSR-amplitudes. The two methods are in excellent agreement for the final $\pi^+\pi^-$ cross section, as can be seen in the upper plot. The relative difference between the two methods is shown in the lower plot. Note: In the upper plot, no correction for vacuum polarization was applied to the pion form factor.

6.1.2 Relative FSR contributions

We use the MC generator PHOKHARA in its current version [11] in order to obtain the relative contribution of LO-FSR and NLO-FSR events to the $\pi^+\pi^-\gamma$ cross section. In Fig. 36 the result for LO-FSR events is shown. Fortunately, the LO-FSR contribution is reduced to values well below 1% over the entire s_π range due to our event selection. FSR photons are preferably emitted along the pion tracks (i.e. at large polar angles) and hence the LO-FSR contribution is highly suppressed. The situation is different for NLO-FSR events as can be seen in Fig. 37. The relative NLO-FSR-contribution is plotted for our kinematical region before and after our trackmass cut. At small values of s_π one finds a relatively large amount of NLO-FSR events before the trackmass cut (up to 4% at $s_\pi = 0.35\mathrm{GeV}^2$). This can be explained by the dominance of events in which radiation from the initial state lowers the invariant mass of the $\pi^+\pi^-$ system to the ρ mass, from which additional final state radiation is then emitted. As can be seen in the plot, a large part of these NLO-FSR events are rejected by the m_{trk} cut.

6.1.3 FSR corrections

In order to obtain the FSR-inclusive cross section $\sigma(e^+e^- \to \pi^+\pi^-)$ from our radiative return measurement, we have worked out two complementary procedures for the FSR-corrections. Both procedures rely on correction functions taken from the PHOKHARA Monte Carlo generator, in which the model of scalar QED has been assumed for the FSR emission. Conceptually, what we do is the following: In the first approach we perform a FSR exclusive analysis, i.e. we take out from our $\pi^+\pi^-\gamma$ spectrum the residual amount of LO-FSR and NLO-FSR events. We then perform the usual event analysis and add the full FSR amount to the cross section $e^+e^- \to \pi^+\pi^-$ at the very end. In the second approach all the analysis is done inclusively with respect to FSR and like that we arrive independently to the FSR inclusve cross section $e^+e^- \to \pi^+\pi^-$.

Before discussing the two procedures in more detail, we remind that in our event analysis only two efficiencies are taken from MC: Acceptance and the trackmass efficiency, while all the other efficiencies are obtained directly from data. Acceptance and trackmass efficiency are however the only efficiencies which are considerably affected by the presence (or absence) of NLO-FSR events. We find differences of up to 5% both for acceptance and trackmass efficiency for a simulation with and without NLO-FSR. Therefore in the exclusive approach the trackmass and acceptance efficiencies are taken from a PHOKHARA production in which only ISR is present, while in the inclusive approach these efficiencies are taken from a PHOKHARA production which contains all the FSR terms shown in Fig. 34. Together with the specific FSR-correction functions described in the following, these are the essential differences between the inclusive and exclusive approach.

Exclusive approach

In the *exclusive* procedure we divide the $\pi^+\pi^-\gamma$ cross section by a correction function $1 + \delta_{\mathrm{IFR}}(s_\pi)$, correcting bin-by-bin the relative amount of FSR at LO and NLO as expected from PHOKHARA after our selection cuts. We introduce like that a fictitious 'FSR-free' cross section $\sigma^{\mathrm{ISR}}_{\pi^+\pi^-\gamma}$. The cross section $\sigma^{all,MC}_{\pi\pi\gamma}$ in the formula below denotes a simulation with the full NLO-ISR + LO-FSR + NLO-FSR contributions, while $\sigma^{ISR,MC}_{\pi\pi\gamma}$

corresponds to the pure NLO-ISR simulation. This correction function corresponds to the curve (after trackmass cuts) shown in Fig. 37.

$$\sigma^{\mathrm{ISR}}_{\pi\pi\gamma}(s_\pi) = \frac{\sigma^{\mathrm{measured}}_{\pi\pi\gamma}(s_\pi)}{1+\delta_{\mathrm{IFR}}(s_\pi)} \quad , \quad \delta_{\mathrm{IFR}} = \frac{\sigma^{all,MC}_{\pi\pi\gamma}}{\sigma^{ISR,MC}_{\pi\pi\gamma}} - 1 \tag{6.1}$$

After this correction step we perform the usual event analysis according to Fig. 4. The acceptance correction and trackmass efficiency are taken from a Monte Carlo production in which only ISR events are simulated. After dividing by the radiator function H, the full (i.e. the real and virtual) FSR-correction corrections to the cross section $e^+e^- \to \pi^+\pi^-$ are applied according to [14], [16]. In the model of scalar QED for FSR-emission this correction is a well known function of s_π and it is rather flat ($0.8\% - 0.9\%$) in the energy range of interest.

Inclusive approach

In the second procedure the analysis is performed *inclusively* with respect to FSR. This time the acceptance and trackmass efficiency are obtained from a FSR-inclusive PHOKHARA production. An additional correction has to be taken into account here, because the invariant mass of the off-mass-shell photon s_{γ^*} is not identical with the invariant mass s_π of the hadronic two-pion-system, the one which is actually measured in the experiment. This correction function is also obtained from Monte Carlo and is shown in Fig. 38. It is actually an unshifting function due to the fact that in the case of real FSR photon emission s_π is systematically lower than s_{γ^*} and we have to correct for this FSR-effect in order to obtain the differential cross section as a function of s_{γ^*}:

$$\frac{d\sigma_{\pi\pi\gamma}}{ds_{\gamma^*}} = \frac{d\sigma_{\pi\pi\gamma}}{ds_\pi} \cdot \epsilon_{unshift} \quad , \quad \epsilon_{unshift} = \frac{d\sigma^{all,MC}_{\pi\pi\gamma}}{ds_{\gamma^*}} / \frac{d\sigma^{all,MC}_{\pi\pi\gamma}}{ds_\pi} \tag{6.2}$$

Comparison

We have analyzed our data according to the exclusive and inclusive approach for FSR corrections and obtain in both cases the cross section $e^+e^- \to \pi^+\pi^-(\gamma_{FSR})$. The relative difference between the two methods shows an agreement $\approx 0.2\%$ as can be seen in Fig. 39. We conclude that the FSR-corrections for the given model of scalar QED are very well under control. We want to stress that this agreement also indicates a posteriori the validity of the assumption of factorization between ISR and FSR (see discussion above) which has been explicitly used during the inclusive procedure for FSR corrections. Finally the comparison gives a valuable cross-check of the entire analysis since we prove that considerably different efficiencies, acceptance and correction functions used in the two approaches do result in an almost identical pion form factor. We assign a systematic uncertainty of 0.3% due to the FSR-corrections discussed in this chapter, where this uncertainty gets contributions from (i) the model dependence of scalar QED and (ii) the uncertainty with which we know the relative contribution of FSR-events. For both individual contributions we assign an error of 0.2% each and add the errors in quadrature. This precision is actually motivated by the agreement between data and Monte Carlo for the charge asymmetry with a relative precision $< 20\%$ which confirms the validity of the model of scalar QED at this level (see Fig. 40). Multiplying this relative uncertainty to the total FSR-contribution of the two-pion cross section ($0.8 - 0.9\%$) we obtain a model error of 0.2%. Concerning the second contribution we simply take the difference between the inclusive and exclusive approach as the systematic uncertainty.

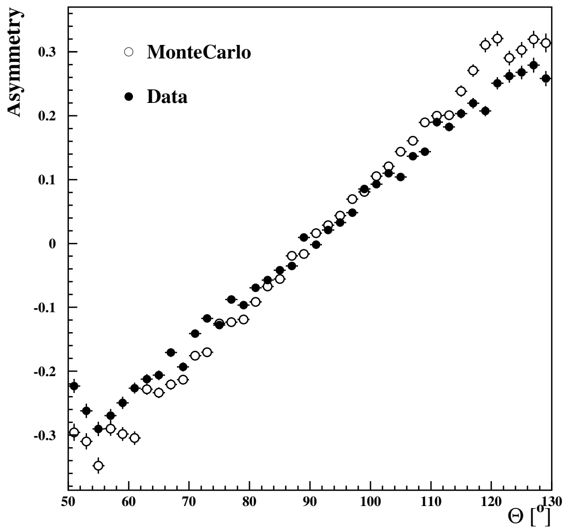

Figure 40: Preliminary results for the charge asymmetry (see Ref. [8]). In the plot the charge asymmetry measured at large photon angles is compared to the MC prediction assuming the model of scalar QED for the FSR emission.

6.2 Vacuum Polarization corrections

In order to obtain the pion form factor, or the *bare* cross section, vacuum polarization effects must be subtracted. This can be done by correcting the cross section for the running of α as follows:

$$\sigma_{bare} = \sigma_{dressed} \left(\frac{\alpha(0)}{\alpha(s)} \right)^2 \tag{6.3}$$

where the running of α can be written as [16]:

$$\alpha(s) = \frac{\alpha(0)}{1 - \Delta\alpha_{lep}(s) - \Delta\alpha_{had}(s)} \tag{6.4}$$

The leptonic contribution can be analytically calculated, while the hadronic contribution stems from a dispersion integral which includes the hadronic cross section itself as integrand:

$$\Delta\alpha_{had}(s) = -\frac{\alpha(0)s}{3\pi} Re \int_{4m_\pi^2}^{\infty} ds' \frac{R(s')}{s'(s'-s-i\epsilon)} \tag{6.5}$$

Therefore, the correct procedure has to be iterative and it should include the same data that must be corrected. However, since the correction is at the few percent level, we have used the $\Delta\alpha_{had}(s)$ as evaluated using $\sigma_{had}(s)$ values measured previously [39]. Table 2 lists the correction used.

7 Results and Conclusions

The cross section for $e^+e^- \to \pi^+\pi^-\gamma$, after applying the corrections described above, is shown in Fig. 41 for $0^o < \theta_\pi < 180^o$ and $\theta_\gamma < 15^o$ or $\theta_\gamma > 165^o$.

In order to get the $e^+e^- \to \pi^+\pi^-$ cross section, the radiation function $H(s_\pi)$ is needed (see Eq. 1.2). The radiator is obtained from PHOKHARA, setting $F_\pi(s_\pi) = 1$ and *switching off* the vacuum polarization of the intermediate photon in the generator. Applying Eq. 1.2, and taking into proper account the FSR contribution using the *inclusive* procedure as described in the section 6.1, the hadronic cross section shown in Fig. 41, right, is derived. Removing FSR and correcting for vacuum polarization as in Tab. 2, the pion form factor shown in Fig. 42 is then obtained using the relation

$$\sigma_{\pi\pi} = \frac{\pi\alpha^2}{3s}\beta_\pi^3 \left|F_\pi\right|^2 , \tag{7.1}$$

where $\beta_\pi = \sqrt{1 - 4m_\pi^2/s}$ is the pion velocity and m_π is the pion mass.

7.1 Results and comparisons with existing data

Our results are summarized in Tab. 3 which shows:

- the cross section $e^+e^-\to\pi^+\pi^-\gamma$ as function of the invariant mass of the dipion system s_π in the angular region $\theta_\Sigma < 15^o$ or $\theta_\Sigma > 165^o$, $0^o < \theta_\pi < 180^o$;
- the physical cross section $e^+e^-\to\pi^+\pi^-$, which includes FSR and vacuum polarization, as function of the invariant mass of the virtual photon s_{γ^*};
- the pion form factor, after removal of FSR and vacuum polarization, as a function of s_{γ^*} (which is equal to s_π in this case since FSR has been removed).

The error is statistical only, while the common systematic error is shown in Tab. 4, Tab. 5 and Tab. 6. Please note that the statistical errors account only for the diagonal elements of the covariance matrix[7], and thus underestimate the actual errors. The covariance matrix must be used for any kind of error propagation (as for example in a_μ calculation, see after).

[7] The covariance matrix is available upon request.

s (GeV^2)	0	1	2	3	4	5	6	7	8	9
0.3...						0.95	0.89	0.84	0.79	0.72
0.4...	0.66	0.60	0.53	0.47	0.40	0.36	0.30	0.27	0.25	0.24
0.5...	0.27	0.32	0.41	0.56	0.73	0.94	1.14	1.34	1.43	1,31
0.6...	1.06	6.79	6.74	5.63	5.01	4.65	4.38	4.19	4.03	3.91
0.7...	3.82	3.73	3.66	3.62	3.63	3.65	3.66	3.64	3.64	3.63
0.8...	3.61	3.60	3.57	3.57	3.53	3.53	3.48	3.43	3.38	3.32
0.9...	3.26	3.18	3.11	3.01	2.89					

Table 2: Correction factor $(\delta - 1) \times 100$ due to vacuum polarization, averaged over 0.01 GeV^2 intervals where the indicated value for s represents the lower edge: $\sigma_{\text{bare}} = \sigma/\delta$.

$s_\pi \vert s_{\gamma^*}$ GeV^2	$\pi^+\pi^-\gamma$ nb/GeV^2	$\pi^+\pi^-$ nb	$\vert F(\pi)\vert^2$	$s_\pi \vert s_{\gamma^*}$ GeV^2	$\pi^+\pi^-\gamma$ nb/GeV^2	$\pi^+\pi^-$ nb	$\vert F(\pi)\vert^2$
0.35	13.40±0.24	330±7	7.68±0.16	0.65	59.40±0.28	714±4	24.69±0.15
0.36	14.59±0.24	349±7	8.26±0.16	0.66	56.38±0.24	657±4	23.05±0.14
0.37	15.78±0.24	370±7	8.92±0.16	0.67	53.04±0.23	595±4	21.18±0.13
0.38	17.04±0.24	392±6	9.60±0.16	0.68	49.87±0.26	543±4	19.57±0.13
0.39	18.63±0.23	416±6	10.35±0.15	0.69	46.98±0.22	493.2±3.1	18.02±0.11
0.40	20.34±0.27	450±7	11.40±0.17	0.70	44.16±0.21	447.0±2.9	16.54±0.11
0.41	22.64±0.24	489±6	12.59±0.16	0.71	41.54±0.19	405.0±2.6	15.17±0.10
0.42	24.56±0.27	521±7	13.63±0.18	0.72	39.05±0.21	367.1±2.6	13.92±0.10
0.43	27.07±0.28	564±7	15.01±0.18	0.73	36.87±0.17	333.3±2.2	12.78±0.08
0.44	29.99±0.27	608±7	16.43±0.18	0.74	35.20±0.18	304.6±2.0	11.81±0.08
0.45	32.65±0.28	649±7	17.82±0.19	0.75	33.22±0.16	277.8±1.8	10.89±0.07
0.46	36.24±0.27	710±7	19.79±0.18	0.76	31.99±0.16	257.2±1.7	10.19±0.07
0.47	40.10±0.29	769±7	21.78±0.20	0.77	30.51±0.17	233.8±1.7	9.37±0.07
0.48	44.34±0.31	830±7	23.86±0.20	0.78	29.60±0.16	217.7±1.6	8.82±0.06
0.49	48.94±0.28	895±7	26.11±0.20	0.79	28.52±0.13	200.3±1.3	8.20±0.05
0.50	54.1±0.4	967±8	28.60±0.23	0.80	27.53±0.14	184.5±1.3	7.63±0.05
0.51	59.77±0.32	1041±7	31.23±0.22	0.81	27.00±0.14	172.1±1.2	7.20±0.05
0.52	64.93±0.32	1102±7	33.50±0.22	0.82	26.48±0.13	160.0±1.1	6.76±0.05
0.53	70.24±0.35	1171±8	36.05±0.23	0.83	25.84±0.15	148.4±1.1	6.33±0.05
0.54	75.6±0.4	1226±8	38.20±0.26	0.84	25.45±0.13	138.5±1.0	5.97±0.04
0.55	80.2±0.4	1279±8	40.32±0.24	0.85	25.16±0.13	129.2±0.9	5.63±0.04
0.56	83.47±0.35	1288±7	41.07±0.24	0.86	24.96±0.12	120.3±0.8	5.29±0.04
0.57	86.06±0.34	1302±7	41.98±0.23	0.87	24.81±0.15	111.8±0.9	4.97±0.04
0.58	87.85±0.34	1297±7	42.36±0.23	0.88	25.09±0.14	106.3±0.8	4.774±0.035
0.59	89.5±0.4	1282±7	42.46±0.24	0.89	25.17±0.12	99.5±0.7	4.516±0.030
0.60	90.31±0.35	1266±7	42.58±0.23	0.90	25.37±0.13	93.1±0.6	4.269±0.030
0.61	74.20±0.35	1006±6	32.43±0.20	0.91	25.86±0.12	87.6±0.6	4.059±0.027
0.62	65.49±0.28	857±5	27.99±0.16	0.92	26.87±0.14	83.0±0.6	3.886±0.026
0.63	64.14±0.28	817±5	27.32±0.16	0.93	27.94±0.14	79.1±0.5	3.741±0.025
0.64	62.09±0.26	772±4	26.27±0.15	0.94	29.49±0.16	75.3±0.5	3.599±0.025

Table 3: $e^+e^-\to\pi^+\pi^-\gamma$, $e^+e^-\to\pi^+\pi^-$ cross sections and pion form factor in 0.01 GeV^2 intervals where the value given indicates the lower bound. Note that while the $\pi^+\pi^-\gamma$ cross section is given as a function of s_π, the $\pi^+\pi^-$cross section and $|F_\pi^2|$ are given as function of the invariant mass s of the intermediate photon γ^*.

s (GeV^2)	0	1	2	3	4	5	6	7	8	9
0.3...						0.8	0.7	0.6	0.6	0.5
0.4...	0.5	0.4	0.4	0.4	0.4	0.4	0.4	0.4	0.4	0.4
0.5...	0.3	0.3	0.3	0.3	0.3	0.3	0.3	0.3	0.3	0.3
0.6...	0.3	0.3	0.3	0.3	0.3	0.3	0.3	0.3	0.3	0.3
0.7...	0.3	0.2	0.3	0.3	0.3	0.3	0.3	0.2	0.2	0.2
0.8...	0.2	0.2	0.2	0.2	0.2	0.2	0.2	0.2	0.2	0.2
0.9...	0.2	0.2	0.2	0.2	0.2					

Table 4: Correlated systematic error in % due to background subtraction in 0.01 GeV^2 intervals. The indicated values for s represent the lower bin edge.

s (GeV^2)	0.58	0.59	0.6	0.61	0.62	0.63	0.64	0.65
δ_{unf}	0.4	0.9	1.4	3.6	0.9	0.8	0.5	0.4

Table 5: Systematic error in % on $d\sigma(e^+e^- \to \pi^+\pi^-\gamma)/ds_\pi$ and $\sigma(e^+e^- \to \pi^+\pi^-)$ due to unfolding in 0.01 GeV^2 intervals. The indicated values for s represent the lower bin edge. Outside this interval the effect is negligible.

<table>
<tr><th></th><th>$\sigma_{\pi\pi\gamma}$</th><th>$\sigma_{\pi\pi}$</th><th>F_π</th></tr>
<tr><td>Acceptance</td><td colspan="3">0.3 % flat in s_π</td></tr>
<tr><td>Trigger</td><td colspan="3">$\exp(0.43 - 4.9 s_\pi) + 0.08$</td></tr>
<tr><td>Reconstruction Filter</td><td colspan="3">0.6 % flat in s_π</td></tr>
<tr><td>Tracking</td><td colspan="3">0.3 % flat in s_π</td></tr>
<tr><td>Vertex</td><td colspan="3">0.3 % flat in s_π</td></tr>
<tr><td>Particle ID</td><td colspan="3">0.1 % flat in s_π</td></tr>
<tr><td>Trackmass</td><td colspan="3">0.2 % flat in s_π</td></tr>
<tr><td>Luminosity</td><td colspan="3">0.6 % flat in s_π</td></tr>
<tr><td>FSR resummation</td><td>-</td><td colspan="2">0.3 %</td></tr>
<tr><td>Radiation function ($H(s_\pi)$)</td><td>-</td><td colspan="2">0.5 %</td></tr>
<tr><td>Vacuum Polarization</td><td>-</td><td>-</td><td>0.2 %</td></tr>
</table>

Table 6: List of completely correlated systematic effects.

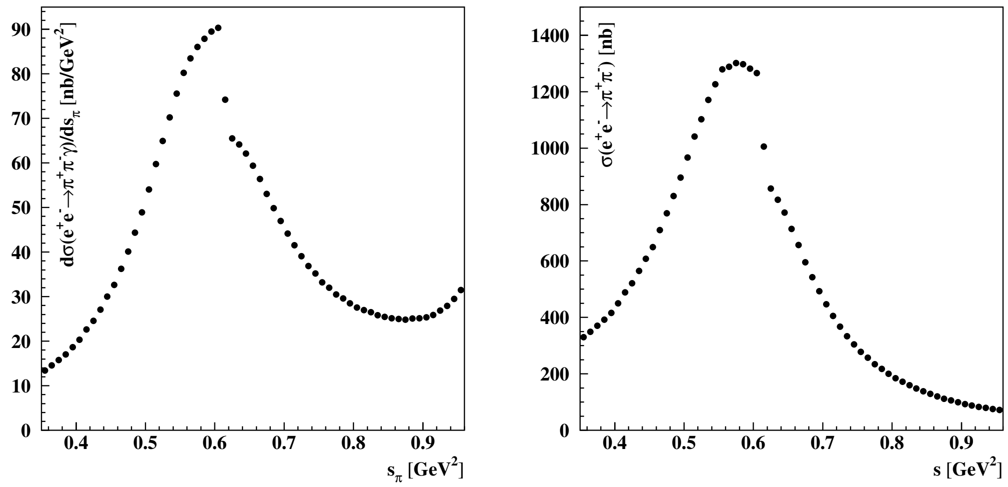

Figure 41: Left: Cross section for the $e^+e^- \to \pi^+\pi^-\gamma$ process, inclusive in θ_π and with $0^o < \theta_\Sigma < 15^o$ or $165^o < \theta_\Sigma < 180^o$. Right: Cross section for $e^+e^- \to \pi^+\pi^-$.

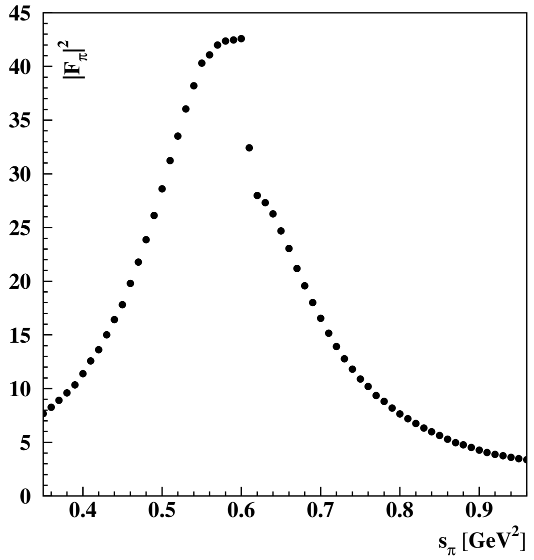

Figure 42: Plot of the pion form factor.

The $e^+e^- \to \pi^+\pi^-$ cross section, divided by the δ factor of Tab. 2, has been used to evaluate the contribution to a_μ^{had} due to the $\pi^+\pi^-$ channel in the energy range 0.35 <

Acceptance	0.3 %
Trigger	0.3 %
Reconstruction Filter	0.6 %
Tracking	0.3 %
Vertex	0.3 %
Particle ID	0.1 %
Trackmass	0.2 %
Background subtraction	0.3 %
Unfolding	0.2 %
Total exp systematics	0.9 %
Luminosity	0.6 %
Vacuum Polarization	0.2 %
FSR resummation	0.3 %
Radiation function ($H(s_\pi)$)	0.5 %
Total theory systematics	0.9 %

Table 7: List of systematic errors on a_μ

$s_\pi < 0.95$ GeV^2. The resulting value (in 10^{-10} units) is :

$$a_\mu^{\pi\pi}(0.35, 0.95) = 388.7 \pm 0.8_{stat} \pm 3.5_{syst} \pm 3.5_{theo} \tag{7.2}$$

The different contributions to the systematic error on a_μ are listed in Tab. 7. To compare with the results from CMD-2, [4], we have integrated a_μ in the range $0.37 < s_\pi < 0.93$ GeV^2 with the following result:

$$\begin{aligned} a_\mu^{\pi\pi}(KLOE) &= 375.6 \pm 0.8_{stat} \pm 4.8_{syst+theo} \\ a_\mu^{\pi\pi}(CMD2) &= 378.6 \pm 2.7_{stat} \pm 2.3_{syst+theo} \end{aligned}$$

The results are in good agreement.

7.2 Conclusions

We have measured the cross section of the process $e^+e^- \to \pi^+\pi^-\gamma$ in the energy region $0.35 < s < 0.95$GeV^2 under the condition that the pion system Σ is emitted at small polar angle with respect to the beam line ($\theta_\Sigma < 15^o$). Using Eq.1.2, we have derived the cross section for the process $e^+e^- \to \pi^+\pi^-$, tabulated in Tab. 3. These values, corrected for the vacuum polarization term of Tab. 2, can be used to derive part of the hadronic contribution to the muon anomalous magnetic moment with a negligible statistical error and with a systematical error of 0.9%(exp) $\oplus$ 0.9%(theo).

Future improvements are expected from data taken in 2002, where more stable background conditions and an improved trigger logic should allow for a considerable reduction of the systematic effects stemming from the offline reconstruction filter and the trigger. A similar upcoming analysis, applied to the events with θ_Σ at larger angles, can probe the energy region down to threshold. Moreover, improvements from the theory side on Monte

Carlo generators both for the luminosity measurement as well as for the ISR process are expected in the near future, which will help to lower the theoretical part of the systematic error.

Acknowledgements

We would like to thank Carlo Michel Carloni Calame, Henryk Czyż, Axel Höfer, Stanislaw Jadach, Fred Jegerlehner, Johann Kühn, Guido Montagna and Germán Rodrigo for numerous useful discussions. We also would like to thank our referees, Stefano Miscetti and Matthew Moulson from the Laboratori Nazionali di Frascati, for countless stimulating input.

References

[1] *Measurement of the negative muon anomalous magnetic moment to 0.7 ppm.*, the Muon $g-2$ collaboration, Jan 2004, submitted to Phys. Rev. Lett., [hep-ex/0401008]

[2] L. Durand, Phys. Rev. **128**, (1962) 441; M. Gourdin and E. de Rafael, Nucl. Phys. **B10** (1969) 667

[3] T. Kinoshita, B. Nižić and Y. Okamoto, Phys. Rev. D **31** (1985) 2108

[4] R.R. Akhmetshin et al. The data were taken in 1994-95 and first presented in hep-ex/9904027. R.R. Akhmetshin et al. Phys. Lett. B 476 (2000) 33; Phys. Lett. B 527 (2002) 161-172

[5] S. Eidelman and F. Jegerlehner, Z.Phys. C **67** (1995) 585

[6] *Updated estimate of the muon anomalous magnetic moment using revised results from e^+e^- annihilation.*, M. Davier, S. Eidelman, A. Höcker and Z. Zhang, Eur. Phys. J. C **31** (2003) 503

[7] G. Cataldi, A. Denig, W. Kluge, S. Müller, G. Venanzoni, published in Frascati Physics Series Vol. XVI (2000), 569

[8] S. Binner, J.H. Kühn, K. Melnikov, Phys. Lett. B **459** (1999) 279

[9] G. Rodrigo, A. Gehrmann-De Ridder, M. Guilleaume, J.H. Kühn, Eur. Phys. J. C **22** (2001) 81;

[10] G. Rodrigo, H. Czyż, J.H. Kühn and M. Szopa, Eur. Phys. J. C **24** (2002) 71

[11] H. Czyż, A. Grzelińska, J. H. Kühn and G. Rodrigo, Eur. Phys. J. C **27** (2003) 563

[12] H. Czyż, A. Grzelińska, J. H. Kühn and G. Rodrigo, Eur. Phys. J. C **33** (2004) 333

[13] K. Melnikov, F, Nguyen, B. Valeriani, G. Venanzoni, Phys. Lett. B 477, (2000) 114

[14] J.S. Schwinger, *Particles, Sources and Fields, Vol.3*, Redwood City, USA Addison-Wesley (1989) 99

[15] V.A. Khoze, M.I. Konchatnij, N.P. Merenkov, G. Pancheri, L. Trentadue, O.N. Shekhovzova, Eur. Phys. J. C **18** (2001) 481

[16] A. Höfer, J. Gluza and F. Jegerlehner, Eur. Phys. J. C **24** (2002) 51

[17] A. Aloisio *et al.* [KLOE collaboration], *The KLOE Detetor, Technical Proposal*, **LNF-93/002** (1993)

[18] M. Adinolfi *et al.* [KLOE collaboration], *The Tracking Detector of the KLOE Experiment*, Nucl. Instr. Meth. A **488** (2002) 51

[19] M. Adinolfi *et al.* [KLOE collaboration], *The KLOE electromagnetic calorimeter*, Nucl. Instr. Meth. A **482** (2002) 364

[20] M. Adinolfi *et al.* [KLOE collaboration], *The trigger system of the KLOE Experiment*, Nucl. Instr. Meth. A **492** (2002) 134

[21] F. Nguyen, *Measurement of the cross section $\sigma(e^+e^- \to hadrons)$ at $Q^2 \in [4m_\pi^2\text{–}1\,\mathrm{GeV}^2]$ with the KLOE experiment*, Ph.D. Thesis, Università degli Studi "Roma TRE", XVI Ciclo

[22] F. Nguyen, *Estimates of background events for the measurement of the differential cross section $d\sigma_{\pi\pi\gamma}/ds_\pi$*. KLOE Memo Nr. 294 (2004)

[23] H. Czyż and E. Nowak, Acta Phys. Polon. B **34** (2003) 5231

[24] G. Alexander *et al.*, Nuovo Cim. A**107** (1994) 837

[25] H. Czyż, A. Grzelińska, J. H. Kühn and G. Rodrigo, [hep-ph/0404078]

[26] M. Incagli, *Trigger and Trigger Veto efficiency for $\pi^+\pi^-\gamma$ analysis*, KLOE Memo Nr. 278 (2002)

[27] S. Müller, *Estimating the FILFO efficiency for the $\pi^+\pi^-\gamma$ small angle analysis using 2001 data*, KLOE Memo Nr. 287 (2004)

[28] B. Valeriani, *A particle identification method for pion-electron discrimination*, KLOE Memo Nr. 295 (2004)

[29] A. Höcker, V. Kartvelishvili, Nucl. Instrum. Meth. A **372** (1996) 469

[30] B. Valeriani, G. Venanzoni, *Unfolding $\pi\pi\gamma$ events*, KLOE Memo Nr. 291 (2004)

[31] C. Bini, *Analysis of the dynamics of the decay $\phi \to \pi^+\pi^-\pi^0$*, KLOE Memo Nr. 274 (2002)

[32] The ALEPH coll., Z. Phys. C **76** (1997) 15

[33] see for example V. Blobel, proceedings of Conference on Advanced Statistical Techniques in Particle Physics, Durham, England, 18-22 Mar. 2003, [hep-ex/0208022]

[34] F.A. Berends, R. Kleiss, Nucl.Phys. B **228** (1988) 537

[35] E. Drago, G. Venanzoni, *A Bhabha Generator for DAΦNE including radiative corrections and ϕ resonance*, **INFN/AE-97/48** (1997)

[36] C.M.C. Calame, C. Lunardini, G. Montagna, O. Nicrosini, F. Piccinini, Nucl.Phys. B **584** (2000) 459

[37] S. Jadach, W. Placzek, B.F.L. Ward, Phys. Lett. B **390** (1997) 298

[38] A.B. Arbuzov et. al., J. High Energy Phys. **10** (1997) 1

[39] $\Delta\alpha_{had}(s)$ points have been provided to us by Fred Jegerlehner. URL http://www-zeuthen.desy.de/ fjeger/alphaQEDn.uu